MAGNETOCONVECTIVE FLOWS AND WAVES IN THE LOWER SOLAR ATMOSPHERE

A THESIS SUBMITTED TO THE DEPARTMENT OF PHYSICS
PONDICHERRY UNIVERSITY

FOR THE AWARD OF THE DEGREE OF
DOCTOR OF PHILOSOPHY

CANDIDATE
C. R. SANGEETHA

THESIS SUPERVISOR
PROF. S. P. RAJAGURU

INDIAN INSTITUTE OF ASTROPHYSICS
BENGALURU - 560 034 INDIA
JANUARY 2017

Declaration

I hereby declare that the material presented in this thesis, submitted to the Department of Physics, Pondicherry University, for the award of Ph.D. degree, is the result of the investigations carried out by me, at the Indian Institute of Astrophysics, Bengaluru, under the supervision of Prof. S. P. Rajaguru. The results reported in this thesis are new, and original, to the best of my knowledge, and have not been submitted in whole or part for a degree in any University. Whenever the work described is based on the findings of other investigators, due acknowledgment has been given. Any unintentional omission is sincerely regretted.

C. R. Sangeetha
Ph.D. Candidate
Indian Institute of Astrophysics
Bengaluru 560 034
January 2017

Certificate

This is to certify that the work embodied in this thesis titled "Magnetoconvective Flows and Waves in the Lower Solar Atmosphere", has been carried out by Ms. C. R. Sangeetha, under my supervision and the same has not been submitted in whole or part for Degree, Diploma, Associateship Fellowship or other similar title to any University.

Prof. S. P. Rajaguru
Thesis Supervisor
Indian Institute of Astrophysics
Bengaluru 560 034
January 2017

Acknowledgements

I sincerely thank my thesis supervisor, Prof. S. P. Rajaguru, for his guidance and support. I am grateful to him for enabling me to participate in various national and international conferences. Also, I am grateful to him for looking into this manuscript in great detail which helped me to bring it to the current form. I am thankful to Dr. B. Ravindra for spending his valuable time to teach me the flct code and for the discussions on tracking velocities and error estimates.

I thank the Director, Indian Institute of Astrophysics (IIA), the Dean and the Board of Graduate Studies, IIA, for providing the facilities to carry out the thesis work and aid in official matters. I acknowledge the use of HYDRA cluster facility at IIA for the computations related to the work presented in this thesis.

I would like to thank my doctoral committee members, Prof. G. Chandrasekaran, Prof. K. B. Ramesh, and Prof. Dipankar Banerjee for their valuable suggestions for the completion of this thesis and also for the timely evaluation of the progress during the Ph. D. tenure. Special thanks are due to Prof. G. Chandrasekaran for guiding and supporting me through the administrative procedures in Pondicherry University (PU) at various stages during Ph.D. I also thank the Dean, School of Physical, Chemical & Applied Sciences, PU, the Head of the Department of Physics, PU, and the staff members of the Department of Physics, PU, for their cooperation in administrative matters.

I am thankful to Dr. Baba Varghese, Mr. Ashok, Mr. Anish Parwage, Mr. Fayaz, the computer center support team, the library staff, the administrative and canteen staff of IIA, and the staff members of Bhaskara hostel and guest house for their help and support.

I am grateful to the SDO/HMI and AIA team for having created such a

marvellous instrument, making the work with its data a joyful experience.

I am indebted to my family, friends, teachers, and all those who directly or indirectly encouraged and helped me in due course.

List of Publications

In International Refereed Journals

1. *Relationships between fluid vorticity, kinetic helicity and magnetic field at the small-scale (quiet-network) on the Sun*
   Sangeetha C. R., & Rajaguru S. P. 2016, ApJ, 824, 120

2. *Lower solar atmospheric wave dynamics over the magnetic-network*
   Sangeetha C. R., & Rajaguru S. P. 2017a, ApJ (In preparation)

3. *Fluid vorticity and magnetic field relations in a small emerging bipolar region*
   Rajaguru S. P., & **Sangeetha C. R.** 2017b (In preparation)

National and International Conference Attended

1. Oral presentation titled 'Relating Photospheric dynamics with Chromospheric emissions UV emissions using SDO/HMI and SDO/AIA (1700 and 1600Å) observations' at COSPAR-2012 held at Mysore.

2. Attended Indo-UK seminar on Solar atmospheric waves studies at IIA in 2012.

3. Poster presentation titled 'Correlation of photospheric p mode absorption with chromospheric UV emissions (in 1600Å and 1700Å wavelength regions)' at Indo-UK meet held at ARIES, Nainital in 2014.

4. Poster presentation titled 'Hemispherical dependence of solar small-scale kinetic and magnetic helicities' at ASI-2015 held at Pune.

5. Oral presentation titled 'Relationships between fluid vorticity, kinetic helicity and magnetic field at the small-scale (quiet-network) on the Sun' at Dynamic Sun - I held at Varanasi.

Abstract

Sun has complex magnetic features like sunspots, magnetic bright points, plages, network fields, filaments, etc. These complex magnetic features are found to be associated with various observed dynamical phenomenons like jets, flares, coronal mass ejections (CMEs), and other eruptive events. Magnetic fields hence play an important role in the dynamics of solar atmosphere. In this thesis, the interaction of fluid flows and waves with the magnetic field in the quiet-Sun is studied.

For the case of flows, the horizontal fluid motions on the solar surface are tracked over large areas covering the quiet-Sun magnetic network from local correlation tracking of convective granules. To derive these motions continuum intensity and Doppler velocity are taken from the Helioseismic and Magnetic Imager (HMI) onboard the Solar Dynamics Observatory (SDO). From these the horizontal divergence, vertical component of vorticity, and kinetic helicity of fluid motions are calculated. With these derived physical parameters, the interaction of magnetic field with fluid motions have been addressed. In our analysis, it has been found that the vorticity (kinetic helicity) around small-scale fields exhibits a hemispherical pattern (in sign) similar to that followed by the magnetic helicity of large-scale active regions (containing sunspots). It has been identified that this observed pattern is a result of the Coriolis force acting on supergranular-scale flows (both the outflows and downflows). Further, it has been observed that the magnetic fields cause transfer of vorticity from supergranular downflow regions to outflow regions, and that they tend to suppress the vortical motions around them when magnetic flux densities exceed about 300 G (HMI). These results are speculated to be of importance to local dynamo action if present, and to the dynamical evolution of magnetic helicity at the small-scale. Also when these analyses are carried out for emerging flux regions, it is found that

the foot points of emerging loops affect the fluid motions around them in a characteristic way implying possible unwinding of built-in twists (helicity) of emerging flux tubes.

For the case of waves, it is found that the p mode power is suppressed in the magnetised photosphere of the Sun and this suppression is calculated in terms of quiet-Sun values (i.e. normalised with respect to the quiet-Sun). These power suppresions are then analysed in relation to the chromospheric emissions in the UV wavelength bands. The phase-shifts of the waves propagating from photosphere (the continuum intensities for photospheric heights are used) to the chromospheric heights (intensities in UV channels of 1600Å and 1700Å) are calculated. Dependences on line-of-sight, total magnetic field strength, and the inclination of magnetic field of p mode power supression, chromospheric emissions in the UV band 1600Å and 1700Å, and of the phase-shifts of the waves propagating from photosphere to lower chromosphere are studied. The energy fluxes are derived from phase-shifts and from cut-off frequencies. These fluxes are compared with one another for consistancy and also are compared with earlier work. At average formation heights 1700Å and 1600Å, the energy fluxes derived from both the methods are found to be $\sim 5 \times 10^6 ergscm^{-2}s^{-1}$ and $\sim 2 \times 10^6 ergscm^{-2}s^{-1}$, respectively for 2-5mHz range. The average chromospheric radiative losses are found to be $\sim 2 \times 10^6 ergscm^{-2}s^{-1}$. Our results hence show that these waves carry sufficient energy to heat the lower solar atmosphere.

The following is the arrangement of the Thesis. Chapter 1 gives an overview of the Sun with focus on the areas mainly related to this thesis. The solar interior and atmospheric structure, different magnetic elements seen on the solar surface, convective motions on the Sun, observed patterns of convection on the solar surface, helicity, oscillations observed in the Sun, heating of solar atmosphere, and lastly observatories used for observation for the completion of the thesis work are discussed in this chapter. The thesis is then divided into two parts: interactions between vortex flows and small-scale magnetic field in the solar photosphere (Chapters 2 and 3), and the effects of waves in chromospheric heating (Chapter 4). In Chpater 2, interactions of fluid motion with magnetic fields are discussed. Chapter 3 focuses on how the fluid motions are affected during flux emergence. Chapter 4 deals with interactions of waves with magnetic fields and effects of

these waves on chromospheric heating. Chapter 5 then presents a summary of the results from all chapters, highlight the novel aspects of this Thesis with its impact and then future work on the basis of the current status of results.

List of Abbreviations

The following is a list of abbreviations used in this thesis, along with their expansions.

SDO. . . . . .Solar Dynamics Observatory
HMI. . . . . .Helioseismic and Magnetic Imager
AIA. . . . . .Atmospheric Imaging Assembly
LOS. . . . . .Line-of-sight
MDI. . . . . .Michelson Doppler Imager
SOHO. . . . . .Solar and Heliospheric Observatory
UV. . . . . .Ultraviolet
LCT. . . . . .Local Correlation Tracking
FLCT. . . . . .Fourier Local Correlation Tracking
CME. . . . . .Coronal Mass Ejections
MHD. . . . . .Magneto-Hydrodynamics
FWHM. . . . . .Full Width at Half Maximum
2D. . . . . .Two-dimensional
VFISV. . . . . .Very Fast Inversion of the Stokes Vector
EFR. . . . . .Emerging Flux Region
NASA. . . . . .National Aeronautics and Space Administration
JAXA. . . . . .Japan Aerospace Exploration Agency

Contents

Chapter 1

Introduction

A central theme in solar physics has been the observational studies of magnetohydrodynamic (MHD) processes on the solar surface (photosphere) and atmospheric layers. Recent advances in observational capabilities, both on ground and in space, have led to a rapid growth in this field. Multi-scale interactions between magnetic fields and plasma motions have been recognised to cause the varied forms of these MHD processes: from the sub-arc-second scale ($\tilde{\text{f}}$ew tens of kilometres) interactions between granular convection and magnetic fields to active regions involving emerging flux that form sunspots and large-scale organisation in the form of supergranular network. A wide temporal and spatial coverage of these processes on the Sun provided by space-borne observatories, e.g. the Solar Dynamics Observatory (SDO), National Aeronautics and Space Administration (NASA) of the USA and the HINODE space-craft of Japan Aerospace Exploration Agency (JAXA), have facilitated wide statistical samplings of these processes thereby enabling probes of fundamental aspects that are otherwise not easily accessible from ground.

This thesis presents a study of certain aspects of magneto-convective interactions between flows, magnetic fields and waves enabled by the continuous (temporal) and full-disk coverage of the Sun by instruments onboard the Solar Dynamics Observatory (SDO); data on velocity and magnetic fields as well as multi-height radiation intensities covering the lower solar atmosphere are used. In the first part, a statistical study on the nature of interactions between vortical flows on the scale of granules, that are advected

by the large-scale supergranular flows, and the small-scale magnetic field distributed all over the Sun – the so called quiet-Sun magnetic network, is presented; in the second part a study of the influence of small-scale magnetic field on the propagation of (magneto-)acoustic waves from the photosphere to the lower solar chromosphere and their energetics are presented.

This Chapter presents introductory material on the Sun followed by that on the topics covered in this thesis. Section 1.1 introduces and summarises basic knowledge on photospheric magnetic structures. Section 1.2 discusses current basic knowledge on granular and supergranular flow fields as observed, and the methods of analyses to derive the fluid dynamical quantities used in this thesis. An introduction to the basic quantities, vorticity and kinetic and magnetic helicities, that describes the dynamics of vortical motions on the solar photosphere is discussed in Section 1.2.1. Waves observed in lower solar atmosphere and the heating mechanisms of the solar atmosphere relevant for this thesis are introduced in Sections 1.3 and 1.4. This Chapter ends with a discussion, in Section 1.5, of the instruments and data from them used in this thesis work.

1.1 The Sun and its magnetic fields

The Sun is the closest laboratory for studying various astrophysical plasma processes in great detail. It has a radius of $\sim 6.96 \times 10^{10} cm$, a mass of $\sim 1.99 \times 10^{33} g$, and an average density of $\sim 1.4 gcm^{-3}$. Its surface temperature is $\sim 6000 K$. The Sun has, at present, about 70% hydrogen, 28% helium and the rest 2% of metals (all elements other than hydrogen and helium are referred as metals). This changes slowly over time as the Sun converts hydrogen into helium through nuclear fusion in its core. The energy generated in the core, which occupies the innermost 20% in radius, diffuses out as radiation through the interior extending up to about 70% in radius from the centre; beyond which the solar structure becomes unstable to convection, which then becomes the dominant form of energy transport in the outer 30% of the Sun. At the photosphere, which is the visible surface layer, the convectively transported energy from below escapes out as radiation into space through the outer atmospheric layers. The photosphere is about 100 km thick, has a temperature and density of $\sim 6000 K$ and $\sim 2 \times 10^{-6} gcm^{-3}$.

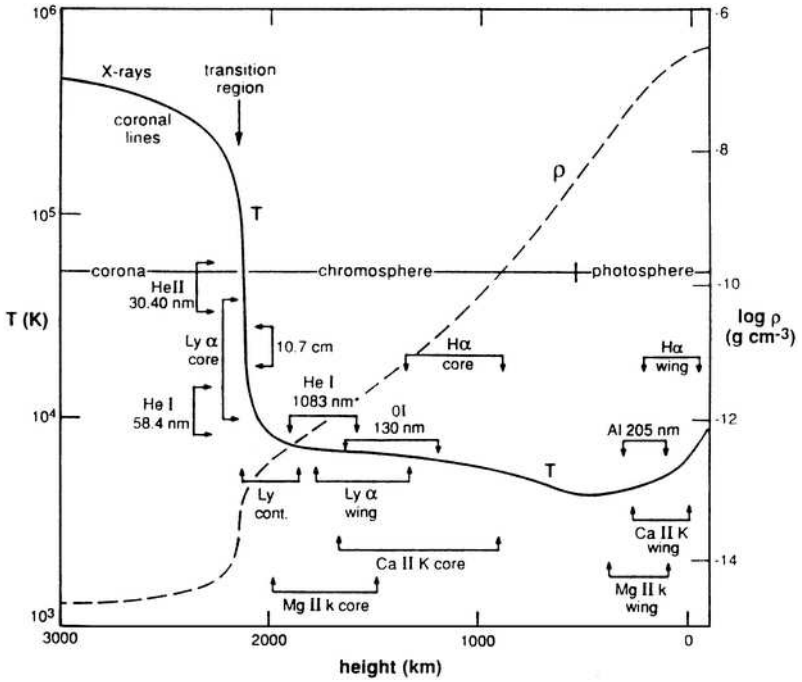

Figure 1.1: The figure shows the variation of temperature and density with height for solar atmosphere. The figure is taken from Avrett (2000).

The temperature in the atmosphere, against height, initially declines passing through a minimum at about $\sim 500km$ from the photosphere, then exhibits a steady rise reaching up to $\sim 10,000K$ over a region called chromosphere that extends to about 2000km; the extended outer layers beyond, called the corona, reach a very hot million K through a thin layer of transition, that is $\sim 500km$ thick. Figure 1.1 shows the variation of temperature and density for different solar atmospheric layers, from photosphere to corona. The density, however, gradually decreases with height. This unique behaviour of the temperature profile is termed as the solar atmospheric heating and will be discussed in Section 1.4. The solar wind is mostly an extension of solar corona in the form of more or less continous outflowing of ions and electrons. It streams off from the Sun in all directions at speeds of $\sim 100kms^{-1}$. The region dominated by the solar wind is called the heliosphere.

Magnetic fields on the Sun are complex and highly variable. The surface phenomena on the active Sun are primarily manifestations of the variable nature of solar magnetic fields. There are a range of time scales for this

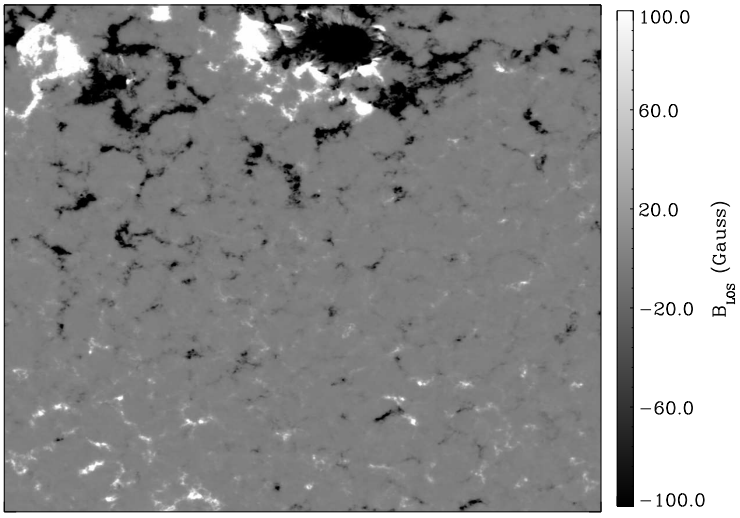

Figure 1.2: The averaged B_{LOS} for an active region used in our work saturated between $\pm 100G$ to make the small-scale network magnetic features visible.

variability, from days, months, years to much longer time scales. The 11 year period for the global solar cycle is the most prominent one, and it is now well recognised that the origin and maintenenace of such variability is due to the operation of a dynamo operating within the solar convection zone. It is also well recognised that the dynamo operation is intimately related to the differential rotation of the 200 Mm deep convection zone including the photosphere: over latitude, the rotation period varies from about 25 days at the equator to about 36 days near the poles; although the bulk of the convection zone rotates at depth independent rates, there is a near-surface shear layer of about 20 Mm thick where the rotation rate increases at all latitudes; the bottom of the convection zone exhibits a very strong and radially thin shear layer, called tachocline, where the latitudinal variation transitions to a near-uniform solid body rotation of the radiative zone Stix (2002).

Sunspots are observed as dark patches in the background of bright intensities in photosphere. Large sunspots typically have temperatures of about 4000 K which is much lower than the temperature in the photosphere, that surrounds the sunspots. Hale (1908) found that these sunspots showed Zeemann splitting which implied that they possess magnetic fields. Modern

observations regularly produce photospheric full-disk magnetograms, which are maps of the magnetic fields or flux densities over the resolution element of the telescope. Sunspots in magnetograms usually appear in pairs of opposite magnetic polarity as seen in Figure 1.2. The white and dark patches seen in the figure indicates the direction of the field, out of the plane and into the plane, respectively. Most of the dynamo theories developed since the original one due to Parker (1955) model the observed bipolar fields to be a result of regenerated toroidal magnetic field in a rotating sphere of conducting fluid, and with a mechanism to build-up and store magnetic flux at the tachocline region (Fan, 2009). The toroidally stretched flux tubes can become buoyant and rise through the convection zone and emerge at the solar surface leading to the formation of sunspots with magnetic field strengths of $\sim 10^3 G$. The appearance of sunspots are usually confined to an equatorial belt ranging between -35° and +35° in latitude. This is often in the form of a leading sunspot, followed by groups of opposite magnetic polarity. The magnetic fields changes direction every 11 years and gains its original configuration every $\sim$ 22 years. When a new solar cycle begins, sunspots tend to appear at high latitudes, but as the cycle progresses towards its maximum, the sunspots appear at lower latitudes. This behavior of sunspots is found to repeat every cycle and is shown as a butterfly pattern when the number of sunspots are plotted as a function of latitude and time (Maunder, 1904).

As mentioned above, sunspots in the intensity maps are seen as dark patches as seen in Figure 1.3. The central dark core is the umbra which is due to strong radial magnetic field. As seen in Figure 1.3, in the periphery of the umbra, fibril like structures are seen and are due to the inclined magnetic field. The umbral diameter of the largest sunspots can exceed 20Mm and penumbral diameter to about 50Mm.

The average magnetic properties of the Sun are not determined by the large-scale fields of the active regions alone but also by the more diffuse areas of magnetic field called the small-scale fields. These are subarcsec to arcsec scale field and are randomly distributed on the surface of the Sun near and away from large-scale magnetic structures. These structures are found all over the Sun. The magnetic flux in quiet-Sun in these small areas are found to have field strength of order $\sim 1kG$ (Stenflo, 1973). These

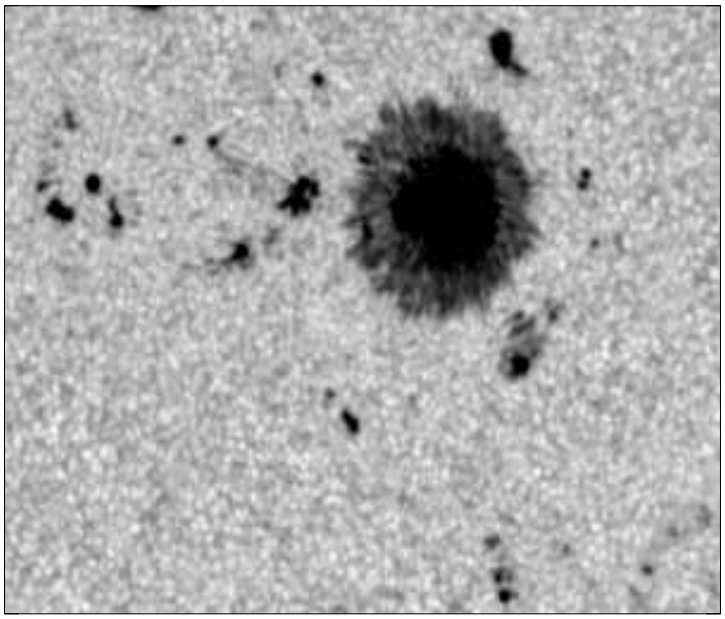

Figure 1.3: The continuum intensity map for an active region used in our work. The white dots seen all over the figure are the granules seen on the photosphere.

structures are found over the entire cycle irrespective of the cyclic behavior of large-scale magnetic activity.

The intergranular lanes are filled with bright plasma trapped in discrete magnetic field as seen below the sunspot in Figure 1.2 forms the magnetic network. These discrete fields are found to be concentrated in the intergranular regions (inflow regions) due to a phenomenon called flux expulsion (Proctor & Weiss, 1982). There have been theories that these discrete fields are generated below the photosphere due to the action of local dynamo or could be due to the dispersal of magnetic flux from active regions and sunspots as they die and the resulting diffusion that arises from the turbulent plasma motions. It is not clear whether one or both determine the observed photospheric distribution of fields and their evolution.

1.2 Material flows on the solar photosphere

The material flows in the solar photosphere is important in understanding the dynamics in the photosphere and also in studying the connections of solar flow fields with the solar atmospheric activities. Local correlation tracking (November & Simon, 1988) is one of the widely used techniques to study the motions of features on the solar surface. DeForest et al. (2007) has compared various feature tracking techniques for the flows in the solar surafce and has found that the results were comparable with each other. In this thesis, we have used a feature tracking code Fouier local correlation tracking technique (Welsch et al., 2004) to derive the flows on the solar surface which is the local correlation tracking in the Fourier space. Part I of the thesis focuses on the flows in the solar surface. Convective motions and the vortical motions observed on the solar photosphere are discussed in this section.

Solar convection is a process where the internal energy and sometimes the latent energy is transported by plasma. They are seen as convective cells, granules, on the solar photosphere. The solar luminosity is mostly transported by fluid motions driven by thermal buoyancy in the solar convection zone. Two major scales of convection seen prominently on the solar surface are those of granulation and supergranulation.

The solar granulation is an intensity pattern with a contrast around 15%, which displays cellular convective motions with length scales ranging from $\sim 0.5 - 2Mm$. These are seen as white dots (at HMI resolution) in the continuum intensity maps as seen in the Figure 1.3. In higher resolution than HMI, these granules are seen to be separated by dark intergranular lanes. The hot plasma moving upwards are seen as white patches and the cooler plasma moving downwards are seen as darker lanes in the intensity maps. The typical lifetime of granules is $\sim$ 10 minutes and that the associated velocities range from $0.5 - 1.5 kms^{-1}$ (Title et al., 1989). The granulation pattern at present is certainly the best understood feature of solar convection and can be reproduced well in numerical simulations. A remarkable property is that the timescales of advection of heat by the velocity field and the radiation of heat are comparable with timescales of granule and thermal dissipation scale.

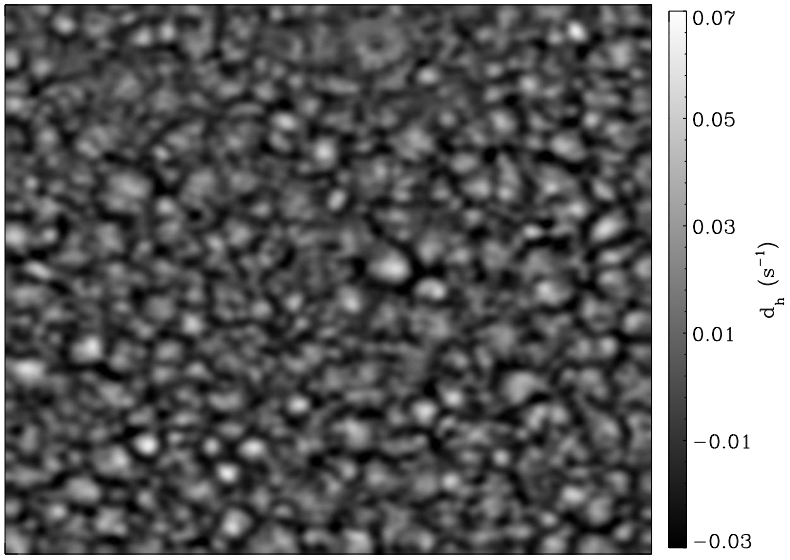

Figure 1.4: The horizontal divergence map derived from horizontal motions tracked from the granular motions of HMI Doppler velocities for a region used in our work. The white patches indicates the outflows while the dark lanes in-between these white patches are the inflows. These dark lanes are the boundaries of the supergranular structures.

The solar supergranulation refers to a physical pattern covering the surface of the quiet-Sun with a typical horizontal scale of approximately 30 Mm and a lifetime of around 27 hours. Its most noticeable observable signature is a fluctuating velocity field of $\sim 0.4 kms^{-1}$ whose components are mostly horizontal. The supergranular boundaries are seen as dark lanes in the horizontal divergence map in the Figure 1.4. Supergranulation was discovered around 1950's (Hart, 1954), however explaining why and how it originates still represents one of the main challenges of modern solar physics. As convective features, supergranules are associated with temperature perturbations that should be visible as an intensity contrast. In practice, such a temperature perturbation is, however, hard to detect in intensity images because it is necessary to disentangle enhanced intensity from temperature perturbations from enhanced intensity due to magnetic fields. According to the convection theory, the size of the convective elements should be proportional to the depth at which they originate. Supergranulation does originate much deeper than granulation where the degree of superadiabaticity

is small. Due to extreme depth of convection, density gradients play an important role in the fluid flow. On the other hand, it might mean that temperature gradients present at the surface are smoothed horizontally by turbulent eddies such as granulation. It is worth considering that supergranulation may not represent free convection at all. It could be caused by Kelvin-Helmholtz instability due to radial shear in the Sun's rotation profile near the photosphere. For a more detailed introduction and current status of supergranulation refer Rieutord & Rincon (2010).

1.2.1 Vortical motions and helicity on the photosphere

Vorticity of a fluid flow is defined as curl of the velocity vector,

$$\omega = \boldsymbol{\nabla} \times \boldsymbol{v} \tag{1.1}$$

where, $\boldsymbol{v}$ is the velocity of the fluid flow. Vorticity is the amount of circulation or rotation in a fluid. Vortical motions on the Sun are found largely in the convective inflow regions, and are known to rotate in counter-clockwise direction in the northern hemisphere and clockwise in the southern hemisphere. The vortex motions observed in solar atmosphere are found to be aligned with the magnetic bright points in the photosphere.

The vortical motions can twist the magnetic flux tubes (Hurlburt et al., 1986). This action of the vortex motion on the magnetic flux tubes can be a mechanism for solar atmospheric heating (Wedemeyer-Böhm et al., 2012). Simulation studies by Stein & Nordlund (1998) have found that the vortex motions were formed by the interaction of plasma fluids with the magnetic fields. These authors also find that the amount of vorticities that are generated in the prescence of magnetic fileds are 4 times larger than the normal fluid case.

Helicity of a vector field, in general, is defined as the volume integral of the scalar product of the field vector and its curl (or rotation) and it quantifies the amount of twistedness in the vector field (Berger & Field, 1984). For fluid flow, the kinetic helicity, H_k, is such a quantity derived from velocity $\mathbf{v}$ and its curl or vorticity, ω,

$$H_k = \int \mathbf{v} \cdot \omega dV \tag{1.2}$$

where dV is the volume element. For magnetic fields, helicity can be calculated in two different ways (Pevtsov et al., 1995): the magnetic helicity, in general, is obtained by applying the above definition on the vector potential $\mathbf{A}$ and its curl (*i.e.*, the magnetic field $\mathbf{B} = \bigtriangledown \times \mathbf{A}$),

$$H_m = \int \mathbf{A} \cdot \bigtriangledown \times \mathbf{A} dV; \tag{1.3}$$

and use of the magnetic field and its curl in the above definition gives the so-called current helicity,

$$H_c = \int \mathbf{B} \cdot \bigtriangledown \times \mathbf{B} dV. \tag{1.4}$$

Both H_m and H_c are measures of twistedness in the magnetic field, and they normally preserve signs over a volume of physical interest (Pevtsov et al., 1995; Seehafer, 1990). Interactions between kinetic and magnetic helicities play fundamental roles in magnetic field generation (or dynamo action) as well as in the magneto-hydrodynamical evolution of the fluid and magnetic field (Brandenburg & Subramanian, 2005; Krause & Raedler, 1980; Moffatt, 1978; Parker, 1955).

The helicities (magnetic, and kinetic) of solar active regions have been extensively studied using observations of the magnetic and velocity fields in and around them. A well known property of the active region magnetic fields is the hemispheric sign rule, originally discovered by Hale (1927) (see also, Pevtsov et al. (1995); Seehafer (1990)); active regions in the northern hemisphere show a preferential negative magnetic helicity while those in the southern hemisphere show positive helicity. The origin or exact cause of such pattern in large-scale magnetic helicity is still not fully understood. Dynamo mechanisms that impart helicity while the field is being generated, as well as transfer of kinetic helicity from fluid motions to the magnetic field as it rises through the convection zone (Longcope et al., 1998) or during and after its emergence at the surface (photosphere), are thought to play roles in the observed pattern (Liu et al., 2014a). On the small scale,[1] away

[1] "Large-scale" and "small-scale" are defined, for the purposes of this thesis, to represent the spatial sizes of coherent magnetic stuctures: large magnetic strcutures such as sunspots are "large-scale", while the smaller structures outlining supergranular boundaries are "small-scale". It is to be noted, however, that these small magnetic structures

from the active and emerging flux regions, the magnetic and kinetic helicities and their interactions are even more poorly understood, as measuring them reliably poses significant difficulties. Although significant advances have been made in mapping horizontal velocities through correlation tracking of surface features such as granulation or magnetic structures (*e.g.*, see Welsch et al. (2007) and references therein), significant uncertainties remain in measuring horizontal components of vector magnetic field at the small-scale (Hoeksema et al., 2014; Liu et al., 2014b) and hence in estimating reliably the current or magnetic helicities there (Y. Liu 2015, private communication; A. Norton, 2016 private communication; see further discussion below.). Observational studies by Duvall & Gizon (2000); Gizon & Duvall (2003) have explored vertical vorticities associated with supergranular-scale flows and such results have guided some theoretical studies of the relations between kinetic and magnetic helicities in the context of turbulent dynamo mechanisms (Rüdiger, 2001; Rüdiger et al., 2001).

Magnetic helicity quantifies how the magnetic field is sheared or twisted compared to its lowest energy state (potential field). Observations provide plenty of evidence for the existence of such stresses in the solar magnetic field and their association to e.g. flare and CME activity, but its precise role in such activity events is far from being clear. Magnetic helicity is one of the few global quantities, which is conserved even in resistive MHD on a timescale less than the global diffusion timescale (Berger, 1984). Thus, as magnetic flux travels from the tachocline through the convection zone, emerges through the photosphere into the corona and is ejected into the interplanetary space during CME events, the magnetic helicity it carries can be traced. It has to be noted that magnetic helicity is different from current helicity, which has been extensively used in establishing the hemispheric helicity rules. While magnetic helicity is, in general, gauge dependent through vector potential $\boldsymbol{A}$, there is no gauge freedom with current helicity. Furthermore, while magnetic helicity is a conserved MHD quantity, this is not the case for current helicity. However, it is usually true that magnetic and current helicities have the same sign. The general relationship between magnetic and current helicities are not known, however, they both are commonly regarded as proxies for twist in magnetic fields.

are distributed on a large-scale all over the solar surface.

1.3 Waves in Solar atmosphere

The first reports on oscillatory motions on the Sun were observed in Dopplergrams in the photosphere (Leighton et al., 1962). It was found that at a given location, the velocity field exhibits a quasi-sinusoidal variation with an amplitude of $\sim 100ms^{-1}$ and a period of around 5 minutes. Studies have been carried out on wave generation, damping, and trapping, mainly in shallow near-photospheric layers. The observed 5-minute oscillations were then interpreted to be the standing acoustic waves trapped in cavities extending well into the interior (Stein & Leibacher, 1974; Ulrich, 1970) and was verified observationally by Deubner (1975). The power distribution in the $k-\omega$ plane by Deubner (1975) fell along well-defined narrow ridges whose shape and position agreed with rich mode structure from the theoretical calculation of the trapped acoustic wave hypothesis.

A perturbation of the hydrostatically supported plasma in the solar interior will generate a spectrum of acoustic (p mode, pressure), or gravity (g mode) waves, or fundamental (f mode, surface gravity) waves, with the dominant restoring force depending on location in the Sun and the perturbation frequency. The observed 5-minute oscillations are the acoustic, p mode oscillations. The dynamics of these oscillations are determined by the variation of the speed of sound inside the Sun. The amplitudes of these p modes at the solar surface are of hundreds of kilometers. These oscillations can be detected with Doppler imaging or sensitive spectral line intensity imaging. g modes are density waves which have gravity (negative buoyancy of displaced material) as their restoring force. They are confined inside the Sun below the convection zone and are practically unobservable at the surface. These g modes are evanescent through the convection zone and are thought to have residual amplitudes of only millimeters at the photosphere. There have been several reported observations of g modes but are not confirmed entirely. f modes are also gravity waves but occur at or near the photosphere, where the temperature gradient again drops below the adiabatic value.

1.4 Heating of Solar Atmosphere

In Section 1.1 it has been seen that the temperature from the photosphere to corona is increasing even though the density is decreasing (see Figure 1.1). This is the heating problem of the solar atmosphere which has been a puzzle to solar physicists. Many heating mechanisms have been proposed over the years which can be broadly classified into two categories: non-magnetic and magnetic. In the non-magnetic heating theory, the acoustic aves are responsible for heating which transforms into shock waves with steep pressure and density gradients in the atmosphere. It is also called the field-free or hydrodynamic or mechanical mechanism. The magnetic heating mechanism is further divided into ac and dc heating. Direct or dc magnetic heating is where a conversion of magnetic energy to kinetic energy happens via Joule heating or magnetic reconnection. Indirect or ac magnetic heating is where the magnetic field lines play the role of a catalyst without being destroyed. In dc heating, the footpoints of the magnetic fields are constantly shuffled by the photospheric granular and supergranular flows, which have random walk characteristics. Due to the high electrical conductivity of the solar atmosphere, the magnetic field lines are frozen-in with the plasma. The magnetic field lines then get twisted and wrapped around each other, which leads to the formation of current sheets in highly stressed regions. When the current in these sheets reaches a threshold value, reconnection sets in, which releases the magnetic energy and can heat up the solar atmosphere. In ac heating models, energy is provided by dissipation of waves in the solar atmosphere. In general, turbulent convective motions on the solar surface generate three different types of waves involving the magnetic field, with waves propagating upwards in the solar atmosphere. These waves are Alfvén waves, fast magnetoacoustic waves, and slow magnetoacoustic waves. The Alfvén waves travel along the magnetic field, while fast and slow magnetoacoustic waves can also travel across the magnetic field. The speed of the magnetoacoustic waves depend on the direction of propagation and on the plasma properties, so these waves reflect against the transition region where there is a large gradient in pressure and density. Thus these waves cannot transport energy from the photosphere to the corona. The natural candidate for heating then are the Alfvén waves (Alfvén, 1947).

Alfvén waves are much more resilient and do not dissipate in the corona except at small-scales. It is thus tough to convert the wave energy into heat.

In this thesis, we have focused on the heating of the lower solar atmosphere. The total radiative loss in the chromosphere is calculated from the summation of the radiated energy in strong chromospheric spectral lines. However, the actual amount of the chromospheric radiative losses is not clear. On the one hand, semi-empirical models predict a rate of $2-4kWm^{-2}$ (Vernazza et al., 1981). On the contrary, a more recent model that includes all iron blends in the wings of chromospheric lines predicts a value of $\sim 14kWm^{-2}$ (Anderson & Athay, 1989).

1.5 Observatories

For this thesis work, data have been used from two major instruments onboard Solar Dynamics Observatory (SDO): Helioseismic and Magnetic Imager (HMI) and Atmospheric Imaging Assembly (AIA). In this section, necessary details on these instruments are discussed. SDO was launched in February 2010 and was injected into a geosynchronous orbit. The data are available online and can be downloaded [2].

1.5.1 SDO/HMI

HMI is an instrument designed to study oscillations and the magnetic field at the solar surface, or photosphere (Scherrer et al., 2012; Schou et al., 2012). It also produces data to enable estimates of the coronal magnetic field for studies of variability in the extended solar atmosphere. HMI observations enable establishing the relationships between the internal dynamics and magnetic activity in order to understand solar variability and its effects. HMI observes the full solar disk in the Fe I absorption line at 6173Å with a resolution of $1''$. HMI provides four main types of data: Doppler velocities, continuum intensities, line-depth, and both line-of-sight and vector magnetograms (Couvidat et al., 2012; Hoeksema et al., 2014). The cadence of first four observables is 45s while the cadence of vector magne-

[2] http://jsoc.stanford.edu/

togram is 120s. HMI is the successor of Michelson Doppler Imager (MDI; Scherrer et al. (1995)) onboard Solar and Heliospheric Observatory (SOHO: Domingo et al. (1995)). The magnetic field measurements in HMI are better than MDI because of the higher Doppler and magnetic sensitivity of the Fe I 6173Å spectral line (Norton et al., 2006).

The observables used from this instrument for the this thesis work are line-of-sight and vector magnetic fields, Doppler velocities, and continuum intensities.

1.5.2 SDO/AIA

AIA is designed to provide an unprecedented view of the solar corona and chromosphere, taking images that span at least 1.3 solar diameters in multiple wavelengths nearly simultaneously, at a resolution of about $1''$ and at a cadence of range 10-24s or better (Lemen et al., 2012). The primary goal of AIA Science Investigation is to use these data, together with data from other SDO instruments and from other observatories, to significantly improve our understanding of the physics behind the activity displayed by the Sun's atmosphere, which drives space weather in the heliosphere and in planetary environments. AIA will produce data required for quantitative studies of the evolving coronal magnetic field, and the plasma that it holds, both in quiescent phases and during flares and eruptions. The wavelength channels observed by AIA are shown in Table 1.1 measuring emissions from upper photosphere to corona.

For the purpose of this thesis, 1700 and 1600Å wavlength channels, which have a cadence of 24s, are used. These wavelengths corresponds to upper photosphere and lower chromosphere regions. The source of 1700Å is in the continuum while for 1600Å is continuum and C IV as shown in Table 1.1.

1.6 Scope of the thesis

As discussed in the previous sections, the interactions between fluid motions and magnetic fields are not fully understood. These interactions play a major role in the observed phenomenon in solar atmosphere and also are

Wavelength	Source	Region of solar atmosphere
1700Å	continuum	Temperature minimum, photosphere
1600Å	C IV + continuum	Transition region, upper photosphere
335Å	Fe XVI	Active region corona
304Å	He II	Chromosphere, transition region
211Å	Fe XIV	Active region corona
193Å	Fe XII, XXIV	Corona, hot flare plasma
171Å	Fe IX	Quiet corona, upper transition region
131Å	Fe VIII, XX, XXIII	Flaring regions
94Å	Fe XVIII	Flaring regions

Table 1.1: The wavelength channels of AIA are on the left column. The second column shows the source of the emissions. The region of solar atmosphere where these emissions are observed are given in the last column.

thought to be a major contributors for the solar atmospheric heating.

One of the major goals of this thesis is to study the nature of interactions between small-scale quiet-network magnetic fields and the vortical fluid motions at the granular and supergranular inflows and outflows, and thereby to quantify the roles of fluid kinetic helicity in imparting helicity to the magnetic fields and vice versa. Further, through a wide spatial coverage over both the hemispheres, the effect of Coriolis forces on the sign of fluid kinetic helicities is also studied. Also, the variation of vorticities with magnetic fields are explored to give some insights on the so-called α-quenching effect due to the back-reaction of the magnetic field on the fluid motion, with implications for any local dynamo action that may be present. The effect of Coriolis force on the supergranular flow in non-magnetised flows are found to be altered during the flux emergence. The dynamo theory predicts that the magnetic flux tubes during their generation at the base of the convection zone have in-built twist or acquire a twist during its emergence in the convection zone due to turbulent convection motions. The change in the vortical motions in the non-magnetised flows could be assumed to be the effect of transfer of twist from magnetic fields to the fluid motions. This gives some insights on the twists that magnetic fields have before their emergence in the photosphere.

Second goal of the thesis is to study the interactions of waves with

magnetic fields, by looking into the effects of p mode power suppression and chromospheric emissions in UV bands with magnetic fields. The energy carried by these waves are found to have maximum in the p mode frequency band. These energy fluxes carried by these waves ($2-5\ kWm^{-2}$) are found to be more than the energy required ($2\ kWm^{-2}$ - radiative losses) to heat the chromosphere in the quiet-network Sun.

The mapping of vorticity in supergranular-scale and also mapping of energy fluxes needs high resolution observations and appropriate analysis technique. In terms of methods, LCT of granules was used to track the horizontal motions from Doppler and continuum intensity signals. The spatial Fourier maps of power of Doppler signals was used to derive p mode power suppression. This thesis is divided into two parts: interactions between vortex flows and small-scale magnetic field, and the effects of waves in lower chromospheric heating. Chapter 2 deals with effects of Coriolis force on vorticity on non-magnetised flows and the effects of magnetic fields on the vortical motions. Chapter 3 deals with the effects of emerging flux on the vortical motions. Chapter 4 deals with lower solar atmospheric heating in the quiet-Sun. In Chapter 5, summary of the work done in this thesis, along with the further directions on future work.

Part I

Interactions between vortex flows and small-scale magnetic field

Chapter 2

Kinetic helicity and magnetic field in the solar photosphere

2.1 Overview

[1]

We derive horizontal fluid motions on the solar surface over large areas covering the quiet-Sun magnetic network from local correlation tracking of convective granules, discussed in Section 1.2, imaged in continuum intensity and Doppler velocity by the Helioseismic and Magnetic Imager (HMI) onboard the *Solar Dynamics Observatory*. From these we study the fluid properties by calculating the horizontal divergence, the vertical component of vorticity, and the kinetic helicity. We study the correlations between fluid divergence and vorticity, and between vorticity (kinetic helicity) and the magnetic field. We find that the vorticity (kinetic helicity) around small-scale fields exhibits a hemispherical pattern (in sign) similar to that followed by the magnetic helicity of large-scale active regions (containing sunspots). We identify this pattern to be a result of the Coriolis force acting on supergranular-scale flows (both the outflows and inflows), consistent with earlier studies using local helioseismology. Furthermore, we show that the magnetic fields cause transfer of vorticity from supergranular inflow regions to outflow regions, and that they tend to suppress the vortical motions

[1] *The work presented in this chapter is published in: Sangeetha, C. R. and Rajaguru, S. P. 2016, ApJ, 824, 120*

around them when magnetic flux densities exceed about 300 G (from HMI). We also show that such action of the magnetic fields leads to marked changes in the correlations between fluid divergence and vorticity. These results are speculated to be of importance to local dynamo action (if present) and to the dynamical evolution of magnetic helicity at the small-scale.

2.2 Introduction

Interactions between turbulent convection and magnetic field in the photospheric layers of the Sun play central roles in structuring and driving varied forms of dynamical phenomena in the atmospheric layers above, and hence in the energetics (see, *e.g.* Nordlund et al. (2009) and references therein). These interactions in the near-surface layers are also basic to local dynamo action (Schüssler & Vögler, 2008), which, if present, could explain the large amount of quiet-Sun magnetic flux inferred from high-resolution observations (Goode et al., 2010; Lites et al., 2008). An important aspect of these interactions is the role of helical or swirly fluid motions which can similarly twist or inject helicity to the magnetic field, and vice versa.

Apart from the above described aspects of interactions between fluid motions and the magnetic field, recently, vortex motions around small-scale magnetic flux tubes and the transfer of helicity from fluid motions to magnetic fields have been identified as key players in the upward energy transport and thus in the heating of solar corona (Wedemeyer-Böhm et al., 2012). While Wedemeyer-Böhm et al. (2012) found vortex flows with lifetimes of about an hour, the numerical simulations of Shelyag et al. (2013) show no long-lived vortex flows in the solar photosphere. Detection of vortex flows at the granular scale in the photosphere date back to the studies by Brandt et al. (1988) and Simon et al. (1989), who infered that such motions could be common features in the granular and supergranular inflow regions. A slightly excess correlation between negative divergence of the horizontal flows (or inflows) and vertical vorticity was found by Wang et al. (1995). Bonet et al. (2008) detected a large number of small vortices in the inflow regions and found a clear association between them and magnetic bright points. Innes et al. (2009) have detected vorticites in the inflow regions by calculating horizonatal flows using ball-tracking technique.

Balmaceda et al. (2010) detected strong magnetic flux at the centers of the vortex flows. Vortical flow maps in the quiet-Sun were calculated by Komm et al. (2007) and circular flow components of the inflows around active regions were calculated by Hindman et al. (2009) using helioseismic ring-diagram technique. A recent work has compared spatially resolved veritical vorticites calculated from two independent techniques, local correlation tracking (LCT) and time-distance helioseismology (Langfellner et al., 2015).

Despite a good number of studies on the vortex flows themselves, there have not been detailed analyses of the relationships between such fluid motions and the magnetic field at the small-scale. For example, there are no reliable inferences on the connections between the helicities of fluid motion and the magnetic field, and on the back-reaction of the magnetic field on the fluid. Much of the difficulty lies in reliably measuring the H_m or H_c of the small-scale magnetic fields, as vector field measurements are often subject to large uncertainties outside sunspots or active regions (Hoeksema et al., 2014; Liu et al., 2014b). For these reasons, there are no reliable measurements to ascertain if the helicity of small-scale magnetic fields follow the hemispheric sign pattern obeyed by active regions. There are conflicting findings regarding the dominant signs of current helicity in the weak or small-scale fields over the hemispheres (Gosain et al., 2013; Zhang, 2006). Helioseismology results on supergranular-scale flows, however, show the effect of Coriolis force introducing a hemispheric sign pattern in the vorticity (and hence kinetic helicity) of supergranular-scale flows (Duvall & Gizon, 2000; Gizon & Birch, 2005; Gizon & Duvall, 2003; Komm et al., 2014; Langfellner et al., 2015).

In this work, we focus on examining how the magnetic field modifies the relationships among the fluid dynamical quantities, divergence, vorticity, and kinetic helicity on the one hand, and how these quantities themselves scale against the strength of the magnetic field on the other. Such an analysis is facilitated by the continuous full-disk coverage of the Sun in velocity (Doppler), granulation (continuum intensity), and magnetic field provided by the Helioseismic and Magnetic Imager (HMI) on board the *Solar Dynamics Observatory* (*SDO*; Schou et al. (2012)). Although the spatial resolution of about 1 arcsec (about 720 km) provided by HMI enables us to track the

granulation features in both the continuum and velocity images, and to derive the horizontal flow field, it is not sufficient to resolve the sub-granular scale vortex flows that possibly surround the tiny magnetic flux concentrations. Hence, the vertical vorticity that we measure from HMI data through LCT of granular motions would have contributions mainly from vortical flows of the size of several granules. Since such flows are likely dominant at the supergranular boundaries and junctions we, in our analyses here, are able to also study the effects of the Coriolis force (Duvall & Gizon, 2000; Gizon & Duvall, 2003) and their influence on the relations between vortex motions and magnetic fields. We discuss the data and the analysis methods in Section 2, the results in Section 3, and provide discussion, conclusions, and notes on future studies in Section 4.

2.3 Data and analysis methods

We have used the three major observables from the HMI on board the *SDO*: Doppler velocities (v_d), continuum intensities (I_c), and line-of-sight (LOS) magnetic fields $B_{\rm LOS}$ (hereafter, we denote $B_{\rm LOS}$ simply as B). The basic data sets are cubes of the above observables over about 19 large regions, typically $30.7 \times 30.7^\circ$ in size (in heliographic degrees, or $373 \times 373\ Mm^2$ with 0.03°/pixel) covering both the northern and southern hemispheres in the latitude range $\pm 30^\circ$and about $\pm 15^\circ$in longitude about the central meridian, tracked for 14 hr and remapped (Postel projected) to a uniform pixel size of $0.5'^{-1}$. The total area covered by the 19 regions on the solar surface is $19 \times 373 \times 373\ Mm^2 = 2.65 \times 10^6 Mm^2$, which is about 0.87 solar hemispheres. The 19 regions chosen are from 11 dates distributed over the years 2010 - 2012. Table 2.1 shows the dates, the hemisphere in which the data is taken, the center coordinates of the the data, and whether sunspot was present in the data. The latitude and longitudes of the center of the data in Table 2.1 are taken from equator and central meridian. Thus the included regions cover equal amount of northern and southern hemispherical areas. Of the 19 regions, 14 are quiet-network regions chosen by examining the magnetograms for the presence of a mixed-polarity network field well away from active regions. The remaining five regions on the five dates as shown in Table 2.1 however, have a sunspot; the data from the first four regions were

Date	Hemisphere	Center co-ordinates	Sunspot
11 July 2010	N	(15°,0°)	No
11 July 2010	S	(-15°,0°)	No
03 August 2010	N	(15°,0°)	Yes
03 August 2010	S	(-15°,0°)	No
08 October 2010	N	(15°,0°)	No
08 October 2010	S	(-15°,0°)	No
03 November 2010	N	(15°,0°)	No
03 November 2010	S	(-15°,0°)	No
08 February 2011	N	(15°,0°)	No
08 February 2011	S	(-15°,0°)	No
19 February 2011	N	(15°,0°)	Yes
19 February 2011	S	(-15°,0°)	No
08 May 2011	N and S	(0°,0°)	No
03 July 2011	N	(15°,0°)	Yes
03 July 2011	S	(-15°,0°)	No
02 October 2011	N	(15°,0°)	Yes
02 October 2011	S	(-15°,0°)	No
21 June 2012	N and S	(0°,0°)	No
02 July 2012	N and S	(0°,0°)	Yes

Table 2.1: The dates of all the observation data is available on the left column. The second column shows in which hemisphere the data is present, North (N), and South (S). The center coordinates from the equator and central meridian of the data used in the analysis in (latitude,longitude) form is given in third column. The last column shows where a sunspot is present in the data.

already available to us and had been used in a different analysis published by the second author (Rajaguru et al., 2013). We included quiet areas of these regions by carefully excluding the sunspots and surrounding plages (one example is shown in Figure 2.1) covering about 8% of the total area, and hence the total quiet-network area included in the analysis is about 0.8 solar hemispheres. Since this discarded area of about 0.07 solar hemispheres is all from the north, we have about 15% more southern hemispherical area over than northern in the analyses here. Figure 2.1 shows two examples from among the analyzed regions: derived flow divergence and vorticity maps overlaid with magnetic field contours (see the following section) over a mixed-polarity quiet-network area (left panels) and over a region covering a sunspot and plages (right panels). The white-line boundaries in the right panel of Figure 2.1 separate the quiet-Sun areas included in the analysis for this region, and these were chosen by visually examining the magnetograms to avoid sunspots and surrounding plages and to include only the quiet-Sun network. These straight-line boundaries are just for convenience and easy inclusion of the chosen areas in the analyses.

We apply the LCT technique (November & Simon, 1988) on v_d and I_c to derive horizontal motions of convective granules. We use the code FLCT (Welsch et al., 2004) that implements LCT through measurement of correlation shifts in the Fourier space. FLCT is applied for two images separated by a time $\triangle t$. Each image is multiplied by a Gaussian of width σ centered at the pixel where velocity has to be derived. Cross-correlation is performed within this Gaussian window to calculate the shifts in the x- and y-directions that maximize the correlation. The shifts in the x- and y-directions are divided by $\triangle t$ to obtain velocities in the x- and y-directions. We remove the f (surface gravity) and p mode oscillation signals in v_d and I_c before applying the LCT to derive fluid motions. This is achieved using a Gaussian tapered Fourier frequency filter that removes frequency components above 1.2 mHz. The FWHM of the Gaussian window for LCT is $\sigma = 15$ pixels and $\triangle t$ is about 2 minute. We apply FLCT at every time-step, *i.e.* every 45 seconds, to derive the horizontal velocity components $v_x(x, y, t)$ and $v_y(x, y, t)$ with the original resolution of the data. One of important test carried out after running LCT code is to see the observed large-scale flow patterns on the Sun can be reproduced from these velocities. The supergranule structure is

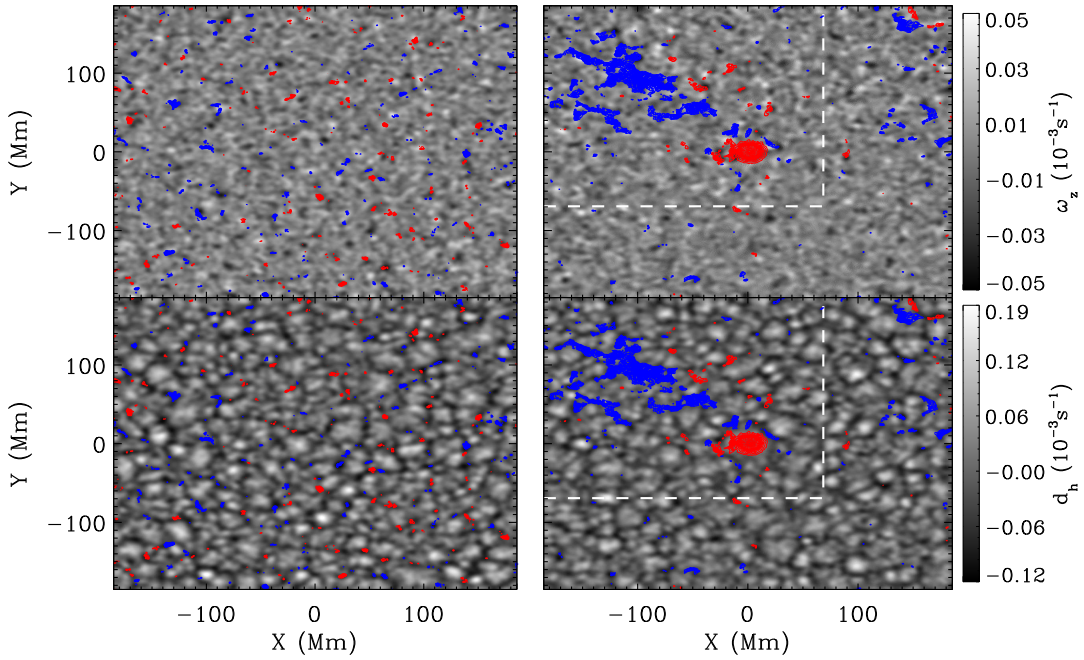

Figure 2.1: Spatial maps of 14 hr averaged vertical vorticities (top panels) and horizontal divergences (bottom panels) derived from LCT of HMI Doppler velocities. The left panels show a region consisting of mixed-polarity quiet-network magnetic fields observed on 2010 November 3 with the map center at latitude 15°S and longitude 0°; the right panels show a sunspot region observed on 2010 August 3 centered at latitude 15°N and longitude 0°. Contours of the magnetic fields averaged the same way are overplotted, showing field values above ± 10 G. The red and blue contours correspond to negative and positive magnetic polarity magnetic fields, respectively. The white dotted lines on the right-hand panels separate the sunspot and plage areas from the quiet-network, which is used in the work presented here.

one of the most well observed pattern on the solar surface. v_x and v_y derived from LCT are tested to see whether they can produce the observed supergranular structure and these velocities are found to reproduce the observed supergranule structure.

From these horizontal components of velocity, we calculate the z-component of the vorticity and the horizontal divergence as,

$$(\boldsymbol{\nabla} \times \boldsymbol{v})_z = \left(\frac{\partial v_y}{\partial x} - \frac{\partial v_x}{\partial y} \right), \tag{2.1}$$

$$(\boldsymbol{\nabla}.\boldsymbol{v})_h = \left(\frac{\partial v_x}{\partial x} + \frac{\partial v_y}{\partial y} \right). \tag{2.2}$$

Calculation of kinetic helicity H_k requires the vertical component of $\boldsymbol{v}$ and its gradient, which we do not have. We follow (Rüdiger et al., 1999) in deriving a proxy for kinetic helicity from the calculated vertical component of vorticity and horizontal divergence,

$$H_{k,proxy} = \frac{\langle (\boldsymbol{\nabla}.\boldsymbol{v})_h)(\boldsymbol{\nabla} \times \boldsymbol{v})_z) \rangle}{\langle (\boldsymbol{\nabla}.\boldsymbol{v})_h)^2 \rangle^{1/2} \langle (\boldsymbol{\nabla} \times \boldsymbol{v})_z)^2 \rangle^{1/2}}. \tag{2.3}$$

This proxy for kinetic helicity is similar to the relative kinetic helicity, $H_{k,rel}$, used by Brandenburg et al. (1995)

$$H_{k,rel} = \frac{\langle \boldsymbol{\omega}.\boldsymbol{v} \rangle}{\langle \omega^2 \rangle^{1/2} \langle v^2 \rangle^{1/2}}. \tag{2.4}$$

in situations dominated by two-dimensional flows.

2.4 Shrinking Sun effect

The velocity maps v_x and v_y calculated from Doppler observations show a systematic variation in x- and y-directions, and the magnitude of change across the spatial extent covered is about $0.4 ms^{-1}$ and this is shown in Figure 2.2. This is attributed to the 'shrinking Sun effect' (Langfellner et al., 2015; Lisle & Toomre, 2004) that shows an apparent disk-centered (or radially directed) inflows. The origin of this constant flow signal (i.e. time independent) is not fully known, although it has been attributed to selection bias of LCT method and to insufficient resolution of the instrument

to resolve fully the granules on the solar surface (Lisle & Toomre, 2004). Lisle & Toomre (2004) have claimed that the LCT method favours the granular motions towards the disk-center since the centers of the granules are more blue-shifted. The redshifted granules in the lanes of inflows are also shown to show this bais, but in the opposite direction. Due to the insufficient resolution of HMI to resolve granules, these granules appear blue-shifted as a whole. Whatever the origin, this constant disk-centered flow signal is easily determined by taking temporal averages (of both v_x and v_y), spatillay smoothing and obtaining a low degree 2-D fit. A thus determined background artifact is then removed by subtracting it out from maps v_x and v_y at every time-step.

2.5 Results: vortical motions, kinetic helicity and the magnetic field

Spatial maps of horizontal divergence, $d_h = (\boldsymbol{\nabla}.\boldsymbol{v})_h$, the vertical vorticity $\omega_z = (\boldsymbol{\nabla} \times \boldsymbol{v})_z$, and the kinetic helicity H_k (hereafter we denote $H_{k,proxy}$ defined above simply as H_k), derived at each time-step as described in the previous section, form our basic fluid dynamical quantities. To improve the signal-to-noise of these measurements, we use a running temporal average over about 4.5 minutes, *i.e.*, average of six individual measurements; this is found to be suitable as the typical lifetime of granules is about 5 - 7 minutes. This running average is taken on the flows derived but not on the cross-correlations of LCT to avoid missing any granular signals that have lifetimes shorter than or close to the averaging interval. An example map of the full 14 hr temporal average of $\mathbf{d}_h$ and ω_z with overlaid contours of similarly averaged B is shown in Figure 2.1.

In this study, we examine (1) the hemispherical dependence of the signs of ω_z or H_k arising from the Coriolis force, (2) how the magnetic field modifies the relationship between d_h and ω_z or H_k, and (3) how these quantities themselves scale against the strength of the magnetic field. Since these quantities are highly dynamic with typical timescales of the order of granular lifetime, we derive the relationship between these quantities at each time-step of measurement. We achieve this by determining, at each time-

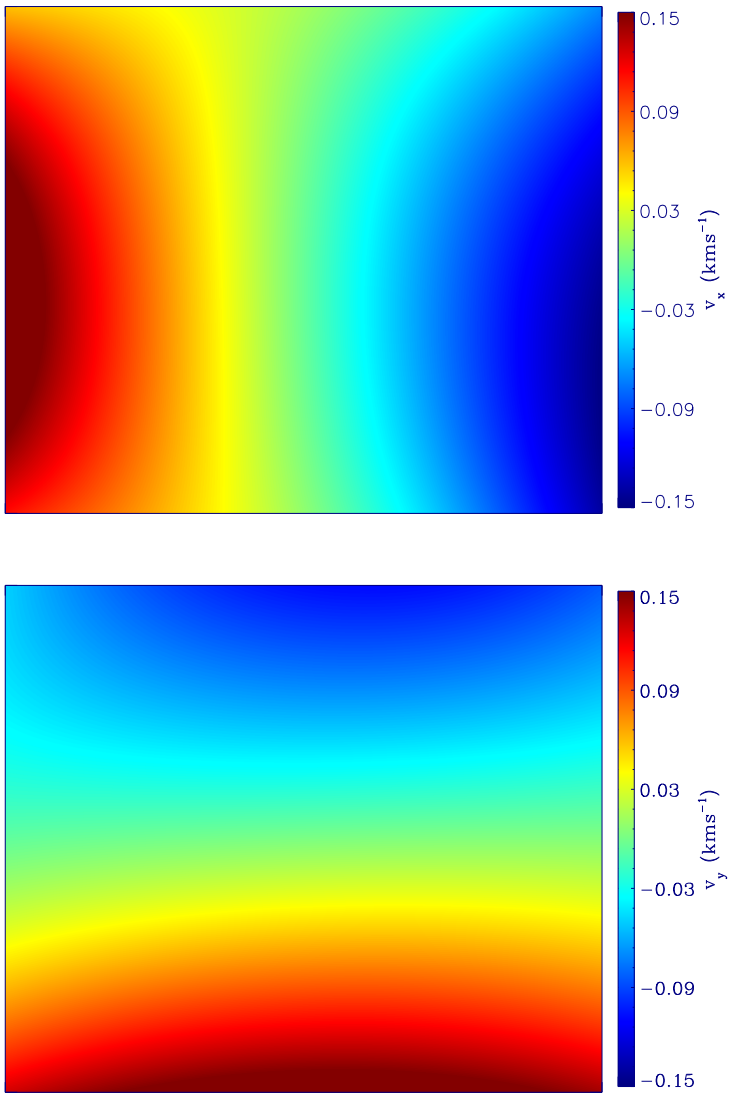

Figure 2.2: The systematic variation in x-direction and y-direction as seen in v_x (top panel) and v_y (bottom panel), respectively for one of the data used for analysis. The velocities, v_x and v_y, shown here are scaled between $\pm 0.15 kms^{-1}$ for easy visualization.

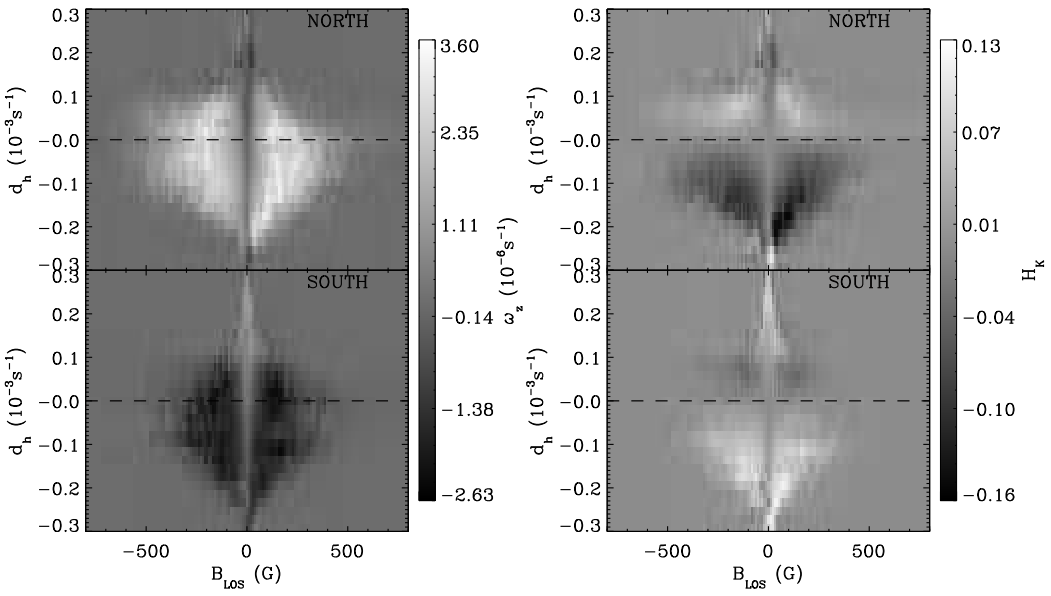

Figure 2.3: Vertical (z-component) vorticity, $\omega_z(d_h, B)$ (left panels), and kinetic helicity, $H_k(d_h, B)$ (right panels), binned against LOS magnetic field, B (x-axis), and horizontal divergence, d_h (y-axis). The results here are calculated from LCT of granular motions imaged in HMI continuum intensities, and are averages over quiet-network in 19 large regions covering the northern and southern hemispheres. See the text for further details.

step, the dependence of ω_z (or H_k) on d_h and B by calculating their average values over chosen small intervals (bin sizes) in B and d_h: 10 G [2] bins in B (a magnetic bin) and 20 μs^{-1} bins in d_h. This is implemented by sub-dividing every magnetic bin, *i.e.*, pixels having magnetic field spread of 10 G, in terms of d_h with a bin size 20 μs^{-1}. We do this for both signed and absolute values of ω_z or H_k, denoting them respectively as $\omega_z(d_h, B)$ or $H_k(d_h, B)$ and $\omega_z^{ab}(d_h, B)$ or $H_k^{ab}(d_h, B)$; in the former case of averages of signed values we perform the calculations for the northern and southern hemispheric regions separately so as to check the hemispheric trends such as those introduced by the Coriolis force, and in the latter case of average of absolute values we combine both hemispheric regions together. The fill-factor for magnetic field is small (*i.e.*, much of the area is occupied by $|B| \approx$ 0 G pixels, see Figure 2.1) and, in general, the area occupied by magnetic pixels decreases sharply as $|B|$ increases (see the bottom panel of Figure 2.4, where a histogram of area, in logarithmic scale, against B is plotted). In such situations a better statistic is provided by median values rather than averages. We tested this by taking median values over the chosen bins of B and d_h and found, however, that the derived relationships are nearly the same for averages and medians.

The above analysis process is repeated for each region, and the average $\omega_z(d_h, B)$, $\omega_z^{ab}(d_h, B)$, $H_k(d_h, B)$, and $H_k^{ab}(d_h, B)$ are thus determined from for all the regions, making sure that the included areas contain only the quiet-Sun magnetic network. The resulting average relationships $\omega_z(d_h, B)$ and $H_k(d_h, B)$ determined for the northern and southern hemispheric regions separately are shown in Figures 2.3 and 2.4: results based on LCT velocities derived using HMI continuum intensities I_c are in Figure 2.3 and those from Doppler velocities are in Figure 2.4, and they agree well. It is seen that the Doppler velocities yield somewhat less noisy results for $\omega_z(d_h, B)$ and $H_k(d_h, B)$ and hence we use these for further analyses in the following Sections. It is to be noted that the signed averages $\omega_z(d_h, B)$

[2]We note that the use of $B = B_{LOS}$ leads to, when much of the magnetic field is vertically oriented on the surface, a systematic bias towards lower field strengths that are about $cos(\theta)$ times the true value for an angular distance of θ° from the disk center. Since the maximum off-center location does not exceed $\theta = 30^\circ$, we have at the most 14% lower values for B. However, average deviations of derived dependences on $B = B_{LOS}$ would differ from true values of B by a much smaller amount than 14%.

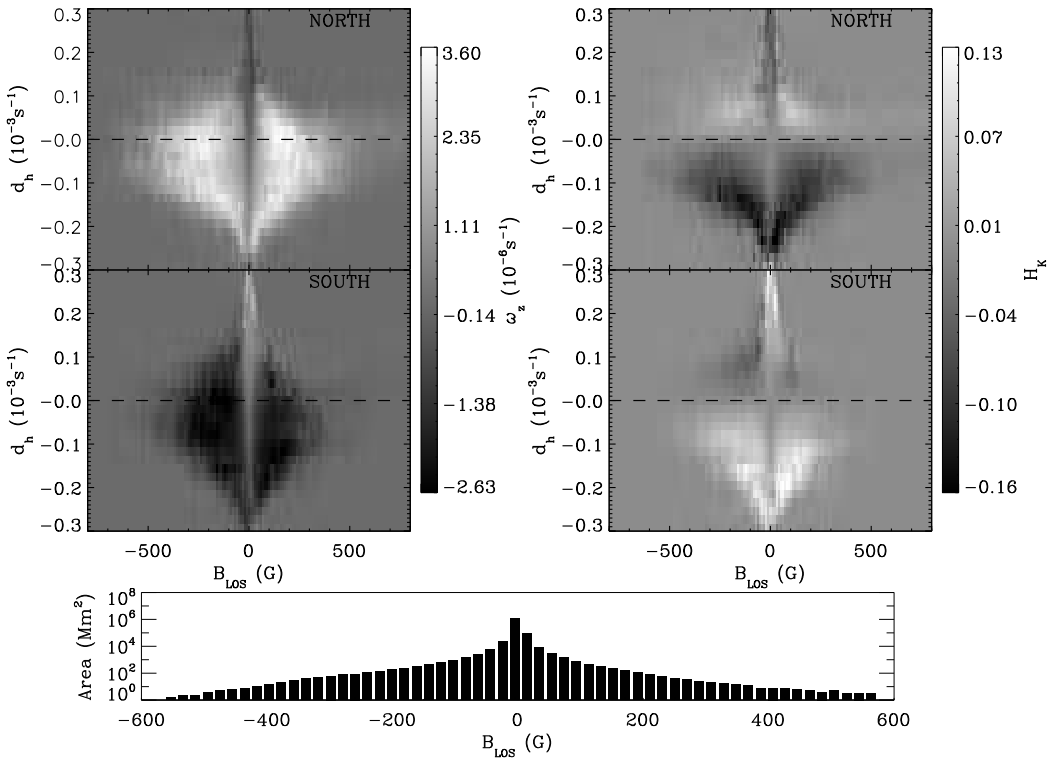

Figure 2.4: $\omega_z(d_h, B)$ and $H_k(d_h, B)$ are the same as plotted in Fig. (2.3) but are derived from correlation tracking of granular motions imaged in HMI Doppler velocities. The bottom panel shows a histogram of area (in logarithmic scale) occupied by magnetic pixels in units of Mm^2 against $B = B_{LOS}$.

($H_k(d_h, B)$) have cancellations and hence measure only the excess of one sign of rotation (either clock-wise (negative) or counter-clockwise (positive) rotation) over the other. Hence, the vanishing of these averages do not necessarily mean absence of rotations, and this is easily checked by the averages of absolute values of $\omega_z^{ab}(d_h, B)$ ($H_k^{ab}(d_h, B)$) shown in Figures 2.7 and 2.8 (a full discussion of results in these figures is deferred to Section 3.1). As can clearly be seen, the excesses $\omega_z(d_h, B)$ ($H_k(d_h, B)$) of one sign over the other are about one-tenth of $\omega_z^{ab}(d_h, B)$ ($H_k^{ab}(d_h, B)$). Further, we see that such cancellations are the largest for non-magnetic (quiet) flows. The dominance of one sign of $\omega_z(d_h, B)$ for flows around magnetised regions is due to the phenomenon of flux expulsion (Proctor & Weiss, 1982) which leads to magnetic flux occupying preferentially the inflow (negative d_h) locations. We discuss this aspect further later in the following Section.

2.5.1 Vorticity - Divergence Correlation: the Effects of Coriolis Force

The results in Figures 2.3 and 2.4 show that, to a large extent, the sign of ω_z (H_k) is positive (negative) or counter-clockwise rotation in the northern hemisphere, and negative (positive) or clockwise rotation in the southern hemisphere. It is to be noted that, in the absence of Coriolis and any other large-scale force, the flows are expected to have a roughly equal distribution of clockwise (negative) and counter-clockwise rotations, and hence a signed average of ω_z or H_k over the magnetic and divergence bins is expected to yield near-zero values due to cancellation among positive and negative vorticities. However, as earlier studies have shown, supergranular-scale flows are indeed subject to Coriolis force and, as the results in Figures 2.3 and 2.4, show that even the smaller-sized inflows (negative d_h) show a predominant hemispheric sign pattern consistent with the Coriolis effect. A closer look at this striking pattern requires understanding first the $d_h - \omega_z$ relationship for the non-magnetic flows.

Quiet-Sun areas devoid of significant magnetic field are captured in the central vertical area close to $|B| = 0$G in Figures 2.3 and 2.4. We take the average of ω_z within $|B| < 15$G, *i.e.*, a horizontal average over three magnetic bins of -10, 0, and 10 G in Figure 2.4, to determine $\omega_z^q(d_h) = \omega_z(d_h, B = 0)$ for the non-magnetic flows. It should be noted that the observational errors in HMI LOS magnetograms are about 10 G (Scherrer et al., 2012) and hence the pixels within $|B| < 15$G can be considered as non-magnetic. The resulting variation of $\omega_z^q(d_h)$ is shown as blue lines in Figure 2.5 (other colored lines in this figure show averages over different ranges of $|B|$, and we discuss them in the next Section). Signed values of ω_z against d_h are shown in the left panel of Figure 2.5, and a comparison of absolute amplitudes of ω_z at inflows and outflows is shown in the right panel by plotting them against absolute d_h. Results plotted similary for H_k are in Figure 2.6. In these figures, we show only the results obtained from LCT velocities derived using HMI Doppler velocities (results obtained from HMI I_c are very similar). The variation of $\omega_z^q(d_h)$ clearly brings out the effect of the Coriolis force on fluid flows on the supergranular-scale, namely a radial outflow (positive d_h) rotates clock-wise (negative ω_z) and a inflow (negative

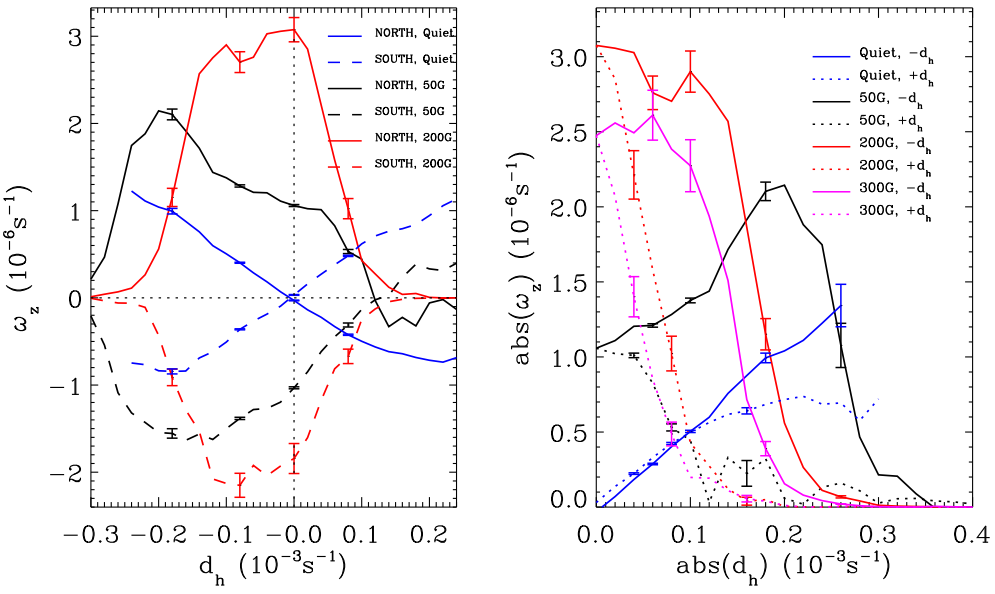

Figure 2.5: Averages over different field strength ranges, as marked in the panels, of vertical vorticities $\omega_z(d_h, B)$ calculated from results shown in Figure 2.4. The left panel shows signed ω_z against signed d_h, whereas the right panel shows the magnitudes of these quantities for an easy comparison of inflow (solid curves) and outflow (dotted curves) regions. The 300 G curves added in the right panel are to show that the vorticity values decrease beyond 200G. They are not shown in the left panel for the sake of clarity as we include both northern and sourthern hemisphere results in the same plot. For the magnitudes in the right panel, we have used those only for the northern region. See the text for further details.

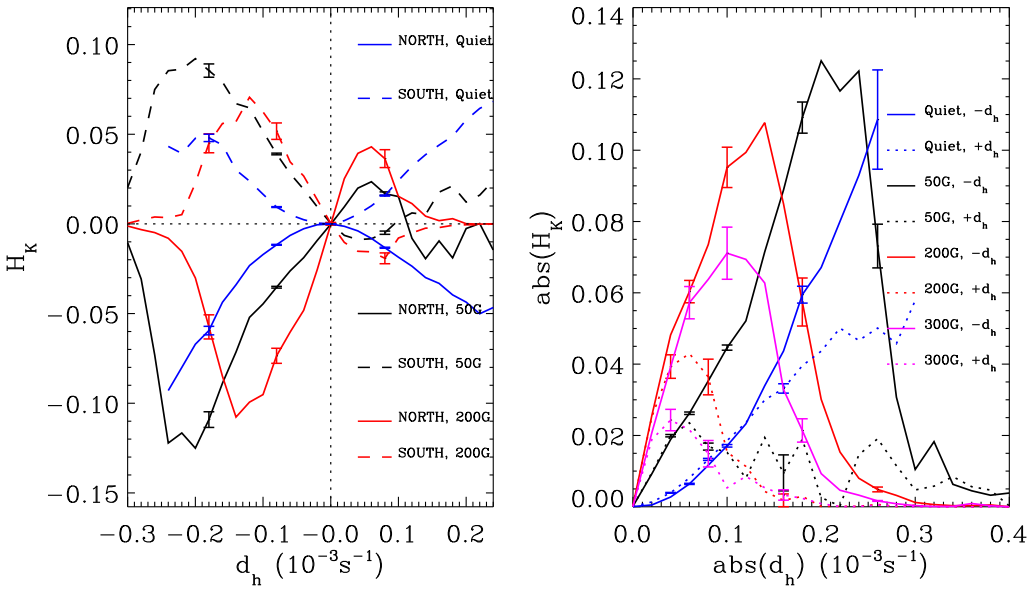

Figure 2.6: Similar plot to Figure 2.5 but for signed averages of kinetic helicity, $H_k(d_h, B)$.

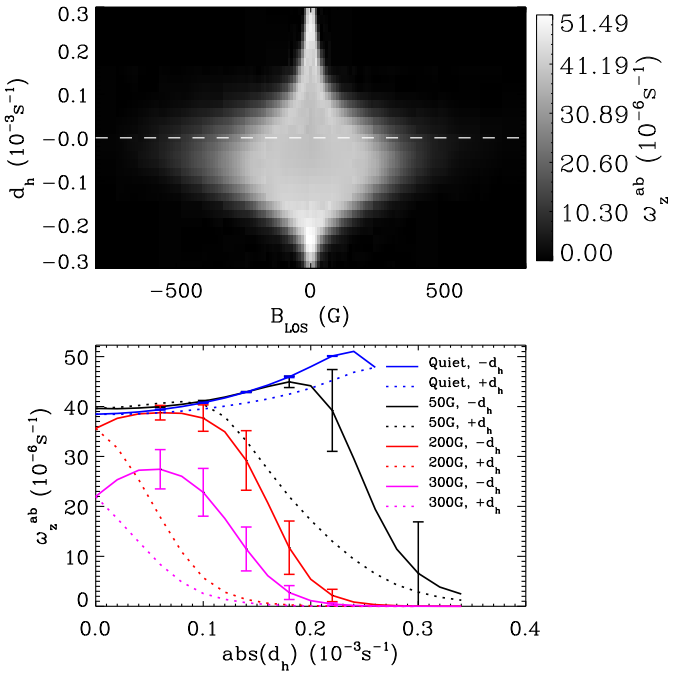

Figure 2.7: Absolute values of vertical (z-component) vorticity, $\omega_z^{ab}(d_h, B)$ (top panel), binned against LOS magnetic field, B (x-axis), and horizontal divergence, d_h (y-axis). The bottom panel shows the cross-sections averaged over different field strength ranges the same as in the right panel of Figure 2.5. See the text for further details.

d_h) rotates counter-clock-wise (positive ω_z) in the northern hemisphere and vice versa in the southern hemisphere. These results are in agreement with earlier known rotation properties of supergranular flows (Duvall & Gizon, 2000; Gizon & Duvall, 2003). Further the magnitudes of ω_z^q derived as above increase more or less linearly against magnitudes of d_h.

Although the above result indicates that the predominant variation of $\omega_z^q(d_h)$ in quiet-Sun flows at the scales that we are measuring is due to the Coriolis effect, it is expected that not all size vortex flows have the signs following the Coriolis effect. In particular, any smaller scale vortex flows at granular inflows or junctions within the supergranular cells can potentially be of larger magnitude and not influenced by the Coriolis force. This indeed turns out to be true as the averages of absolute values, $\omega_z^{ab}(d_h, B)$ ($H_k^{ab}(d_h, B)$), shown in Figures 2.7 and 2.8 portray. The top panels in these

figures show the 2D binned maps, while the bottom panels show the non-magnetic $\omega_z^{ab,q}(d_h)$ (blue lines) and averages over a few selected magnetic field ranges (as in Figures 2.5 and 2.6) against abs(d_h) for a comparison of outflows and inflows. In the analysis and plots here, the error bars represent standard deviations within the ranges of the magnetic bins used. First, as noted earlier, the magnitudes of vorticities (determined through the averages of absolute values) are about ten times those of the excesses determined to be resulting from the hemispherical preference of one sign over the other due to the Coriolis force (comapre the values in Figures 2.5 and 2.6 with those in Figures 2.7 and 2.8). The magnitudes of vorticities estimated in our work here compare very well with earlier local helioseismic results from Duvall & Gizon (2000); Gizon & Duvall (2003), and with the local helioseismic as well as LCT analyses of Langfellner et al. (2015). Second, in agreement with the earlier findings (Wang et al., 1995), the inflow regions have slightly excess vorticity (and helicity) compared to the outflow regions for non-magnetic flows (the blue curves in Figures 2.7 and 2.8). We discuss the magnetic modifications in the following Section.

2.5.2 Magnetic effects: Transfer and Redistribution of Vorticity

To study how the above described non-magnetic relationship $\omega_z^q(d_h)$ is influenced by the magnetic field, we average $\omega_z(d_h, B)$ and $\omega_z^{ab}(d_h, B)$ (as well as $H_k(d_h, B)$ and $H_k^{ab}(d_h, B)$) over three different ranges of magnetic field: 20 - 80 G (denoted as 50 G), 150 - 250 G (denoted as 200 G), and 250 - 350 G (denoted as 300 G) centered around 50, 200 and 300 G. The results are shown in the Figures 2.5 - 2.8. First, we see from Figures 2.3 and 2.4 that the sign of $\omega_z(d_h, B)$ over the magnetized regions does not follow the dependence on d_h expected from the action of the Coriolis force: while the non-magnetic ($< \pm 10$G) central vertical regions of Figures 2.3 and 2.4 show the sign change (the blue curves in the left panel of Figure 2.5) through d_h = 0., the magnetised regions show predominantly one sign, *i.e.*, positive in the north and negative in the south, which should hold only for inflows or converging flows (negative d_h) if the Coriolis effect is the cause. However, magnetic fields over outflows or diverging flows (positive d_h) also show the

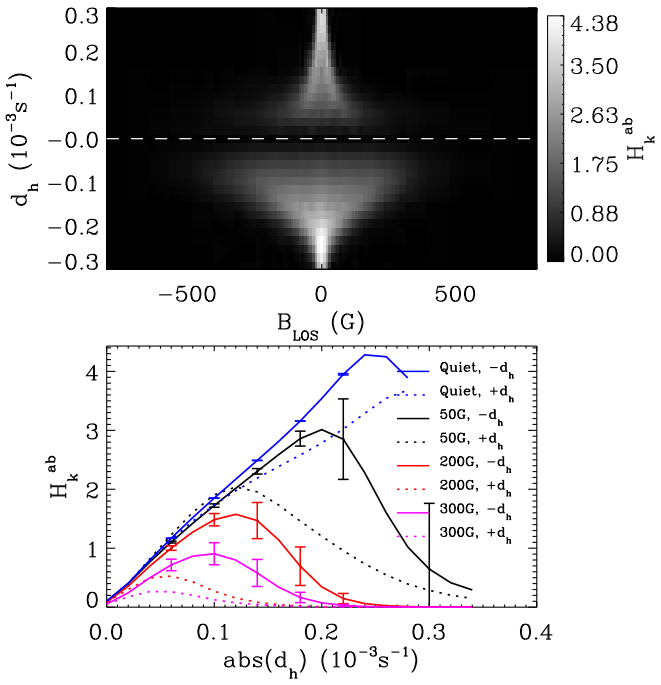

Figure 2.8: Similar plot to Figure 2.7 but for averages of absolute values of kinetic helicity, $H_k^{ab}(d_h, B)$.

same sign as that seen over converging (negative d_h) regions, although it is noted that the majority of the magnetic fluxes lie over the coverging or inflow (negative d_h) regions. It is clear that the dominantly inflow located magnetic fields are connected to those located in the interiors of supergranules (with positive d_h), and that such connectivity transfers vorticity from the inflow (negative d_h) regions to fluid surrounding such connected fields within the supergranules (positive d_h). This magnetic connectivity is expected in the predominantly mixed-polarity flux, which can have a large horizontal component or loops arching above the photosphere. This transfer can happen in either direction, but it is seen in Figures 2.3 and 2.4 that the tranfer of vorticity (and kinetic helicity) is predominantly from inflow regions (negative d_h) to outflows or diverging flows (positive d_h); this is consistent with the fact that stronger magnetic fields with larger fluxes are found mainly over the inflow regions. The cross-sections over the three different magnetic field ranges plotted in Figures 2.5 - 2.8 show the above described signatures of transfer of vorticity from inflow to outflow regions more clearly, and also show how the strengths of the magnetic field influence this phenomenon.

We add a caveat here to the above inferences on possible transfer of vorticity from supergranular inflow (negative d_h) to outflow (positive d_h) regions: the rearrangement of magnetic flux during the process of evolution of supergranules, namely "dying" inflow that is replaced by the outflow of a new supergranule, can lead to our analyses finding vorticity in outflow regions that matches the vorticity in inflow regions (as described above). This can arise because the newly formed outflow (in the place of old inflow) has not had time to sweep the flux to the new inlfow region and the Coriolis force too has not had time to act and hence reverse the vorticity. However, we note that the averaging over 14 hours, which is more than about half the lifetime of a supergranule and hence is long enough for both the above processes to establish, should tend to smooth out such signatures of dying and newly forming supergranular flows. Nevertheless, a residual signature of this process is certainly possible in our analyses.

In addition, we find that these differences between inflow and outflow vorticities (and helicities) are much more pronounced for flows around magnetic fields – see the black (50 G), red (200 G), and pink (300 G) curves in

Figures 2.7 and 2.8. It is to be noted, however, that these enhanced excesses of inflow vorticities, both in signed averages (Figures 2.5 and 2.6) as well as in averages of absolute values (Figures 2.7 and 2.8), also depend on the fact that much of the magnetic fields, in particular stronger concentrations, are located in inflow regions. This is clearly seen in the 2D maps in Figures 2.3 and 2.4 and in the top panels of Figures 2.7 and 2.8, which show the large asymmetry in the areas occupied by non-zero vorticities in the $B-d_h$ region: relatively weaker fields are found in the supergranular outflows (positive d_h), and the majority of the magnetic flux and stronger field concentrations are in the inflow (negative d_h) regions. A basic feature in all the above magnetic effects is that the linear relationship characterizing $\omega_z^q(d_h)$ has given way to more complicated variations. We present and describe the dependences on the magnetic field strength further in the following section.

2.5.2.1 Magnetic Suppression of Fluid Vorticity and Helicity

To examine the influence of magnetic field strengths on the sign and amplitudes of ω_z and H_k (Figure 2.4), and on the absolute magnitudes of ω_z^{ab}, and H_k^{ab} (top panels of Figures 2.7 and 2.8), we take the averages of these quantities over the divergence bins. These results are shown in Figures 2.9 and 2.10. As noted earlier, at $|B|$=0 G, the opposite contributions to ω_z and H_k from the positive (outflow) and negative (inflow) d_h regions cancel out, yielding near-zero values for these quantities. However, the averages of the absolute values of ω_z^{ab} and H_k^{ab} show that the largest magnitude vorticities are to be found over non-magnetic flows, and they decline sharply as $|B|$ increases. The excesses $\omega_z(B)$ and $H_k(B)$, however, show a rapid increase at low magnetic field strengths, reaching a maximum between about 150 and 200 G. The sign pattern of magnetic field correlated ω_z and H_k preserves that expected from Coriolis force action on inflows (negative d_h regions). Taken together, these results show that a major contribution to the larger magnitudes of vorticities and kinetic helicities in inflow regions, compared to those over diverging flows in the interiors of supergranules, leading to the hemispheric excesses seen in Figure 2.9 are due to the predominance of magnetic fields at inflow locations. It is also possible that the supergranular inflows have more vigorous swirls around them due to larger thermal

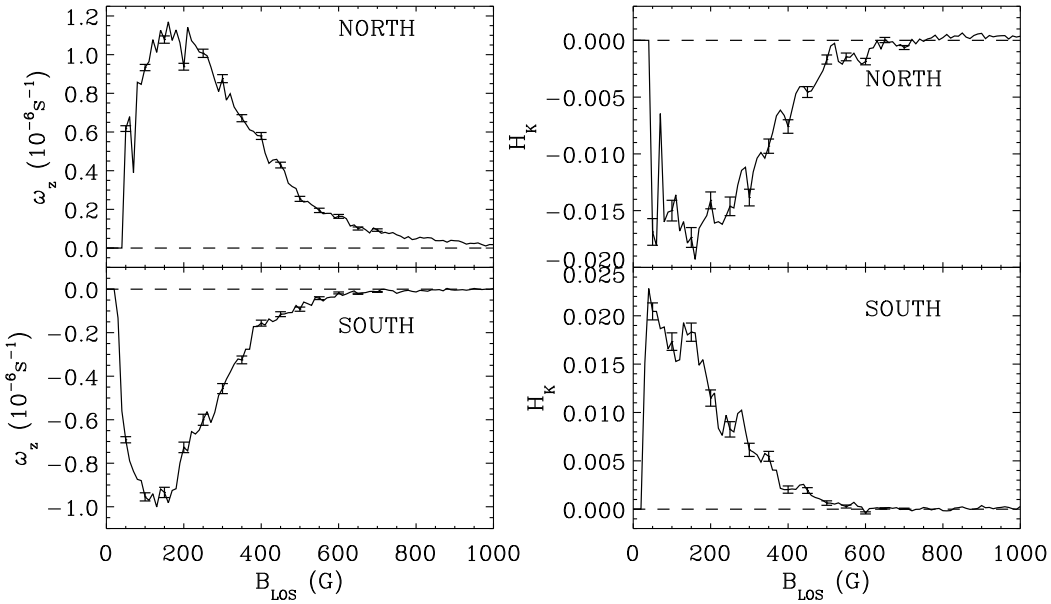

Figure 2.9: The left panels show vertical vorticities, $\omega_z(B)$, averaged over the divergence bins in Figure 2.4, plotted against field strength $|B|$ for the northern and southern hemispheres separately. The right panels show the similarly averaged kinetic helicities $H_k(B)$. The error bars represent standard errors estimated from individual measurements. Horizontal dashed lines in the panels mark the zero level of the ordinates.

perturbations that strong magnetic flux concentrations cause in the solar photospheric layers: cooler magnetic field trapped photospheric gas acts as channels for further heat (radiative) loss, vertically outwards accelerating the flows surrounding hotter plasma toward them, thus enabling stronger inflows and vorticities.

As the magnetic field increases further beyond equipartition strength, which is typically about 300 - 400 G for the solar photosphere, the back-reaction of the magnetic field via the Lorentz force, involving both the pressure and tension forces, acts to inhibit the flows. This effect eventually becomes dominant and acts to compensate the contributions from the Coriolis force assisted combinations of inflows and magnetic fields leading to the decreases seeen in Figure 2.9. As to the averages of absolute magnitudes ω_z^{ab} and H_k^{ab} shown in Figure 2.10, it is clear that, when we ignore

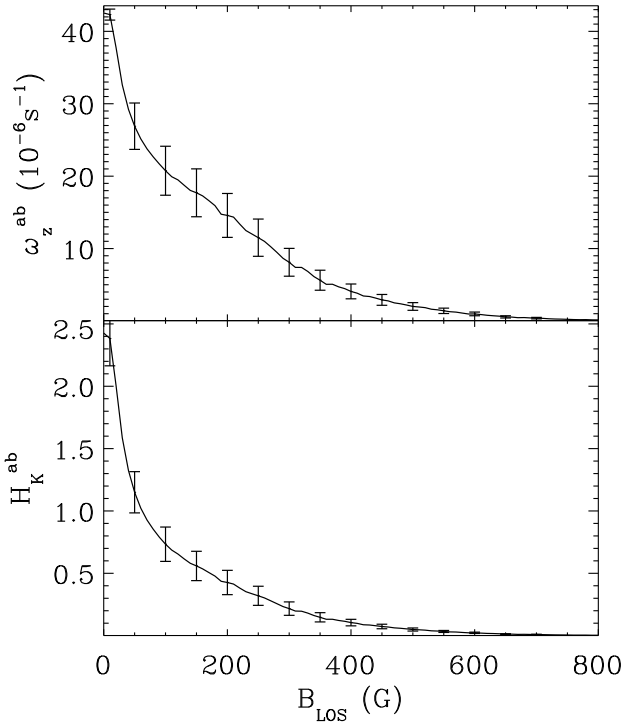

Figure 2.10: The same as Figure 2.9, but for averages of absolute vorticties, $\omega_z^{ab}(B)$ (top panel), and kinetic helicities $H_k^{ab}(B)$ (bottom panel). Here, the north and south regions have been averaged together.

the outflow - inflow asymmetry in the magnetic field locations and the resulting influence of the Coriolis force, the net effect of magnetic forces is to suppress vortical motions. There might also be contributions due to the fact that field strengths B here (from HMI) are flux densities within the resolution element of the instrument, and hence the increase of $|B|$ here may mainly reflect the increase of flux while the actual field strengths are already in strong saturated super-equipartition values. That the photospheric small-scale network field concentrations outlining supergranular inflows are predominantly of super-equipartition kG field strengths is a well established fact. Hence, the results in Figure 2.10 for vorticities and kinetic helicities may correspond to the so-called highly α-quenched state, if photospheric flows are considered for a (helical-) turbulent local dynamo (see, *e.g.*, Brandenburg & Subramanian (2005) and references therein). In nonlinear mean-field dynamo theory, both the hydrodynamic (α_k) and magnetic (α_m) parts of the the α-effect are coupled via the magnetic field, and explicit algebraic expressions for the dependences $\alpha_k(B)$ and $\alpha_m(B)$ are available (Rogachevskii & Kleeorin, 2000; Zhang et al., 2006). The α_k is proportional to H_k^{ab} shown in Figure 2.10. However, we note that the theoretical quenching functions that determine $\alpha_k(B)$ are in terms of the mean magnetic field B, which develops out of dynamo action at the small-scale, whereas in our observations and analysis here B refers to the field at the small-scale. A more detailed look at $H_k^{ab}(B)$ or $\alpha_k(B)$, their spectra, both spatial and temporal, and their relations to various other local and global properties of solar magnetic fields in the context of dynamo mechanisms is beyond the scope of the work reported here. Moreover, higher spatial resolution than provided by HMI to resolve sub-granular scale flows and magnetic fields is important to address such details.

2.6 Summary and Discussion

We have derived and analyzed horizontal fluid motions on the solar surface over large areas covering the quiet-Sun magnetic network using LCT of convective granules imaged in continuum intensity and Doppler velocity by the HMI onboard *SDO*. We have studied the relationships between fluid divergence and vorticity, and that between vorticity (kinetic helicity) and

the magnetic field. These relationships are derived through both signed and absolute averages of ω_z and H_k over time and space. These latter dependences are studied through fluid divergence $d_h(x, y, t)$ and the magnetic field $B(x, y, t)$, yielding $\omega_z(d_h, B)$, $H_k(d_h, B)$, $\omega_z^{ab}(d_h, B)$, and $H_k^{ab}(d_h, B)$ (Figures 2.3 - 2.6). The main results obtained can be summarised as follows.

(1) The correlations between the vorticity and divergence of non-magnetic flows at the supergranular-scale have the dominant hemispheric sign pattern brought about by the action of the Coriolis force. The rotations of outflows and inflows are roughly of equal magnitude and of opposite sign, although there is a slight excess of inflow vorticities which increase as the magnitude of divergence increases. Further, the non-magnetic vorticities scale linearly with the divergences.

(2) For magnetised flows, the sign pattern corresponding to the inflows dominates over the whole divergence field, *i.e.*, even the outflow regions (positive divergence, interiors of supergranules) exhibit the rotations expected from the action of the Coriolis force acting on inflows. In other words, for magnetised flows the dominant sign pattern is negative helicity H_k (positive ω_z) in the north and positive helicity H_k (negative ω_z) in the south. We have identified and attributed this to the mechanism of transfer of vorticity from network inflow regions to interiors of supergranules by the magnetic connectivity or by the horizontal component of magnetic field, with a caveat that supergranular evolution ("dying" inflow that is replaced by the outflow of a new supergranule) can also contribute to the observed signatures.

(3) The excess of inflow vorticities over those of outflows increases dramatically for magnetised flows. This has been identified as due to the preferential inflow locations of the magnetic fields resulting from the convective flux expulsion mechanism. The contributions of instrinsically larger rotations of inflows around stronger fields there due to thermal causes, however, can also play a role in the above asymmetries between outflow and inflow rotations.

(4) In terms of the absolute magnitudes of vorticities, it has been found that non-magnetic flows have the largest values. As a function of magnetic field strengths, as observed by HMI, the magnitudes of absolute vorticities

decrease almost exponentially, causing the magnetic suppression of flows due to Lorentz forces. In particular, we find that the magnetic fields largely suppress the amplitudes of vortical motions when magnetic flux densities exceed about 300 G (from HMI). This magnetic suppression of vorticities or helicities is identified as that arising from the α-quenching action of the magnetic field. This identification is found reasonable as much of the magnetic flux in the solar photosphere is known to be of kG strengths, which are well above the equipartition values.

The above results have wider implications and relations to several other related phenomena pertaining to magneto-convective processes in the solar photosphere. The results (1) and (2) above related to the hemispheric pattern of fluid kinetic helicity and its relationship to the magnetic field are of importance in understanding the transfer of helicities between the fluid and magnetic fields, in particular in situations where reliable measurements of magnetic helicities in the small-scale are difficult to obtain. Since we have not measured magnetic helicities, we cannot establish the connections or transfer of helicities between fluid motions and the magnetic field. However, if the transfer of helicities happens between fluid motions and the magnetic field, irrespective of which direction it happens, we expect both to have the same sign. In our analysis, we find that kinetic helicity is negative (positive) in the northern (southern) hemisphere and this is consistent with magnetic helicity followed by active regions. On the other hand, if the small-scale fields have the opposite sign of current helicity compared to active regions as reported by Gosain et al. (2013), then the transfer of helicity from fluid motions could not have happened, as this is not consistent with our observations. Thus, if the magnetic helicity of the small-scale magnetic fields all over the Sun has contributions from kinetic helicity, then we expect it to have the same sign as the active regions. Hence, our results indicate that small-scale magnetic helicity would indeed be of the same sign as that of active regions that follow the usual hemispheric trend.

The transfer and redistribution of vorticities by magnetic fields implied by results (2) and (3) exemplify the basic magnetohydrodynamic effect known from early laboratory experiments involving conducting liquid metals performed and expounded by Shercliff (1971). These same laboratory experiments also demonstrate the suppression of swirly motions by the mag-

netic field, when the field and fluid velocity directions are not aligned. Our result (4) here is an example for this phenomenon on the Sun.

As regards the relevance of our results for understanding the nature of fluid turbulence and the associated dynamo-sustaining state of near-surface convection (Brandenburg & Schmitt, 1998; Rüdiger, 2001), we note that the dominance of negative kinetic helicity in the north, and hence the expected same sign for magnetic helicity, indicate a positive α-effect in the north in contrast to that required for explaining the observed butterfly diagram of large-scale active regions. As referred to earlier, more detailed analyses of the distribution of kinetic helicity, its interactions with the magnetic field, its spatio-temporal spectra, and their relations to various other local and global properties of solar magnetic fields are necessary to make progress toward devising observational diagnostics of possible dynamo actions happening in the near-surface layers. We note that continuous wide field of view observations of higher spatial resolution to resolve sub-granular scale flows and magnetic fields than provided by HMI/*SDO* is important to address such details. We believe that the kind of analyses undertaken here, *e.g.*, such as those derived from the results in Figure 2.4, as applied to magnetic regions in different dynamical states such as emerging flux regions, decaying active regions, and those before, during, and after major atmospheric activity such as eruptions or flares, would aid in understanding the interactions between fluid and magnetic helicities, their evolution, exchange, and transport upwards in the atmosphere.

Chapter 3

Fluid vorticity and magnetic field relations in a small emerging bipolar region

3.1 Overview

[1]

We derive horizontal fluid motions on the solar surface around an emerging bipolar region from local correlation tracking of convective granules imaged in continuum intensity and Doppler velocity by the Helioseismic and Magnetic Imager (HMI) onboard the *Solar Dynamics Observatory*. From these we study the fluid properties by calculating the horizontal divergence, the vertical component of vorticity, and the kinetic helicity are studied during emergence. The correlations between fluid divergence and vorticity, and between vorticity (kinetic helicity) and the magnetic field get altered during the flux emergence. We find that the hemispherical pattern observed in vorticity (kinetic helicity) around small-scale fields is influenced by the dynamic evolution of the fields. We identify this pattern to be a result of the influence of emerging flux acting on supergranular-scale flows (both the outflows and inflows). Furthermore, we see that the magnetic fields transfer their built-in or pre-emergence twists/helicity to the fluid flows around them. We

[1] *The work presented in this chapter is in progress and will soon be submitted to a refreed journal*

also show that such action of the magnetic fields leads to marked changes in the correlations between fluid divergence and vorticity in non-magnetic regions.

3.2 Introduction

The magnetic fields are generated by the so-called solar dynamo, which also predicts that the magnetic fields possess an built-in twist during its generation. Also theories state that magnetic fields, during their emergence in the convection zone, acquire twists due to turbulent convective motions in the convection zone (Liu et al., 2014a). The magnetic twist of the magnetic flux tubes is observed in various structures in solar atmosphere (Martínez González et al., 2016; Park et al., 2016; Wedemeyer-Böhm et al., 2012; Zaqarashvili et al., 2015). The magnetic helicity is a conserved quantity even in resistive magnetohydrodynamics (Berger, 1984) which means it could be detected even in the coronal mass ejections seen in the interplanetary space (van Driel-Gesztelyi et al., 2003). It is difficult to measure magnetic helicity on the Sun, so usually current helicity is derived on the Sun. It conserves the sign as magnetic helicity in most of the cases. This twist in the magnetic fields are assumed to interact with the fluid motions on the solar surface, and due to this interaction the helicity transfer from magnetic flux tubes to fluid motions or vise-versa is assumed to take place. The fluid motions on the Sun also possess the so-called kinetic helicity due to Coriolis force acting in the fluid motions. The interaction between the fluid helicity and the magnetic helicity is still not observed and confirmed *i.e.,* no studies have been carried out to study these interactions on the Sun.

During flux emergence on the photosphere, we would expect the interactions between fluid motions and magnetic fields to take place. In other words, one can hope to see that transfer of helicity from magnetic fields to fluid motions or vise-versa to happen during flux emergence. This could also be true for cases of cancellation of flux elements or interactions of flux elements to form new or different magnetic structures on the Sun. Keeping this in mind, in this work, we perform similar analysis as presented in Chapter 2 to study interactions between fluid motions and magnetic fields during flux emergence of a bipolar region in the southern hemisphere of

the Sun. Due to coriolis force acting on the supergranular-scale motions the vorticity and diverence are already found to be correlated as reported in Chapter 2 and as known earlier (Duvall & Gizon, 2000; Gizon & Duvall, 2003; Sangeetha & Rajaguru, 2016). This correlation is also found to be affected in the prescence of magnetic field (Chapter 2 (Sangeetha & Rajaguru, 2016)). By carrying out the analysis done in Sangeetha & Rajaguru (2016), we can see some effects of the interaction of magnetic field during its emergence on the fluid vorticity. We discuss the data and the analysis methods in Section 2, the results in Section 3, and provide discussion, and conclusions in Section 4.

3.3 Data and Analysis

We have used Doppler velocities (v_d), continuum intensities (I_c), and line-of-sight (LOS) magnetic fields $B_{\rm LOS}$ (hereafter, we denote $B_{\rm LOS}$ simply as B) as the observables from HMI on-board *SDO*. The basic data sets are cubes of the above observables are over large area for 3 days, 2011 May 8, 9, and 11, typically 30.7 × 30.7° in size (in heliographic degrees, or $373 \times 373\ Mm^2$ with 0.03°/pixel) covering both the northern and southern hemispheres in the latitude range ±15°and about ±15°in longitude about the central meridian, tracked for 14 hr and remapped (Postel projected) to a uniform pixel size of $0.5'^{-1}$. The emerging flux region appears in the southern hemisphere and the analysis is carried in this region covering an area of $91 \times 54\ Mm^2$. This area was chosen visually by looking at the magnetogram data for all the three dates. Figure 3.1 shows the analyzed regions: derived flow divergence and vorticity maps overlaid with magnetic field contours of the emerging flux area.

The LCT technique (November & Simon, 1988) is applied using FLCT code (Welsch et al., 2004) on v_d and I_c to derive horizontal motions of convective granules in the same manner as done in Sangeetha & Rajaguru (2016) (Refer to the paper for more details; hereafter called as Paper I). From these velocities, the vertical component of vorticity, ω_z, the horizontal divergence, d_h, and kinetic helicity, H_k, are derived as in Paper I.

Figure 3.2 shows the magnetic field measurements for the 3 dates of observation. On 2011 May 8 the emergence starts and is found to be con-

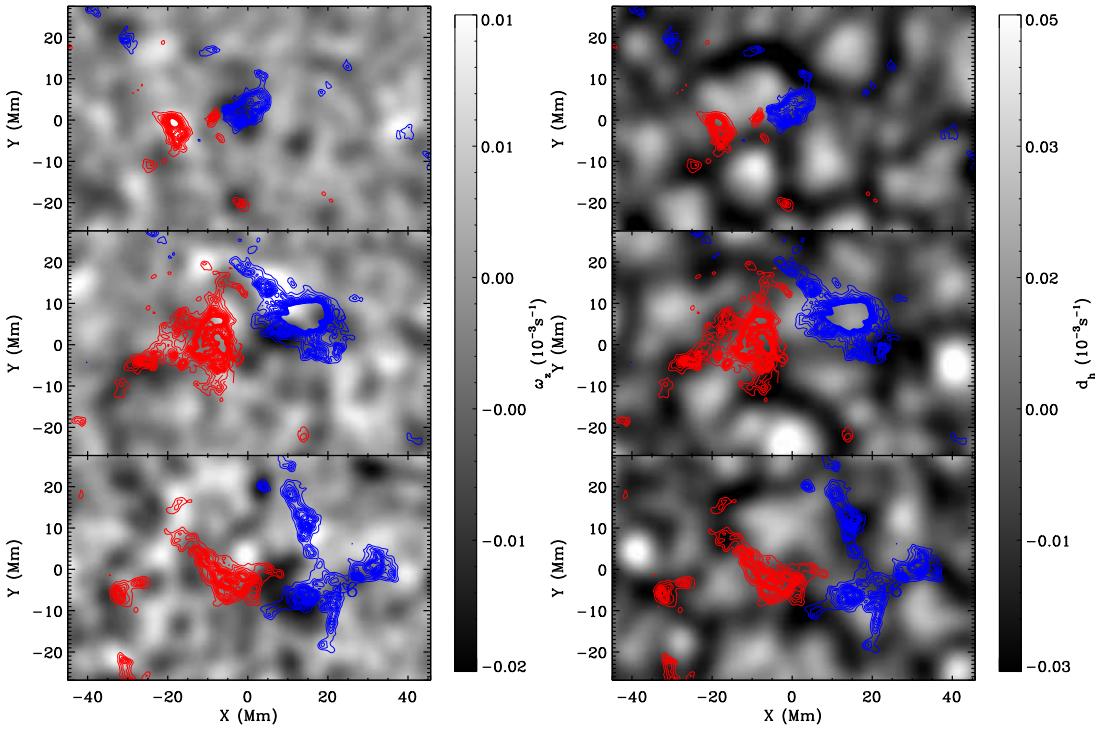

Figure 3.1: Spatial maps of 14 hr averaged vertical vorticities (left panels) and horizontal divergences (right panels) derived from LCT of HMI Doppler velocities. The top panels show for 2011 May 8; the middle panels show for 2011 May 9; the bottom panels show for 2011 May 11 for an emerging flux region. Contours of the magnetic fields averaged the same way are overplotted, showing field values above ± 10 G. The red and blue contours correspond to negative and positive magnetic polarity magnetic fields, respectively.

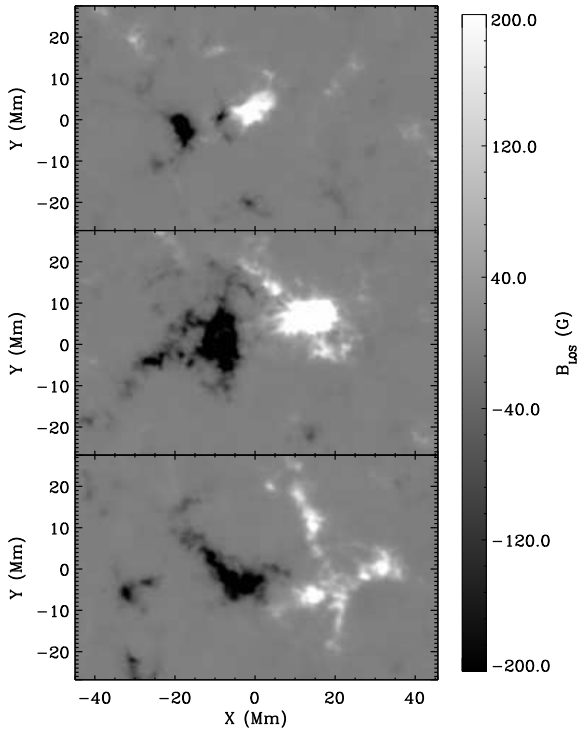

Figure 3.2: Spatial maps of B_{LOS} averaged over 14 hr for 2011 May 08 (top panel), 09 (middle panel), and 11 (bottom panel).

centrated in a smaller area, but the field strength is found to be high. On 2011 May 9, and 11 the magnetic fluxes are seen to be more diffused.

3.4 Results

To improve the signal-to-noise of these measurements, we use a running temporal average over about 4.5 minutes, as in Paper I. This running average is taken on the flows derived but not on the cross-correlations of LCT to avoid missing any granular signals that have lifetimes shorter than or close to the averaging interval. Also the systematic variation found in the velocities are removed from the velocity maps as discussed in Paper I. A map of the full 14 hr temporal average of $\mathbf{d}_h$ and ω_z with overlaid contours of similarly averaged B is shown in Figure 3.1 for the 3 dates.

In this study we examine,

1. the alteration in hemispherical trend of ω_z (H_k) due to the emerging flux,

2. how this emergence affect the correlation between ω_z (H_k) and d_h,

3. time evolution of ω_z during flux emergence.

During the flux emergence, these fluid dynamical quantities, and magnetic field are highly dynamic and their interaction is studied at every time step of measurement. We achieve this by determining, at each time-step, the dependence of ω_z (or H_k) on d_h and B by calculating their average values over chosen small intervals (bin sizes) in B and d_h: 10 G bins in B (a magnetic bin) and 20 μs^{-1} bins in d_h. This is implemented by sub-dividing every magnetic bin, *i.e.*, pixels having magnetic field spread of 10 G, in terms of d_h with a bin size 20 μs^{-1}. We do this for signed values of ω_z or H_k, denoting them respectively as $\omega_z(d_h, B)$ or $H_k(d_h, B)$; in the averages of signed values we perform the calculations in the regions close to the emerging flux which appears in the southern hemisphere so as to check the hemispheric trend introduced by the Coriolis force observed in Paper I where southern hemisphere preferentially show negative sign for ω_z (clockwise rotation).

The above analysis process is repeated for the 3 dates for the same region. The resulting average relationships $\omega_z(d_h, B)$ and $H_k(d_h, B)$ determined for

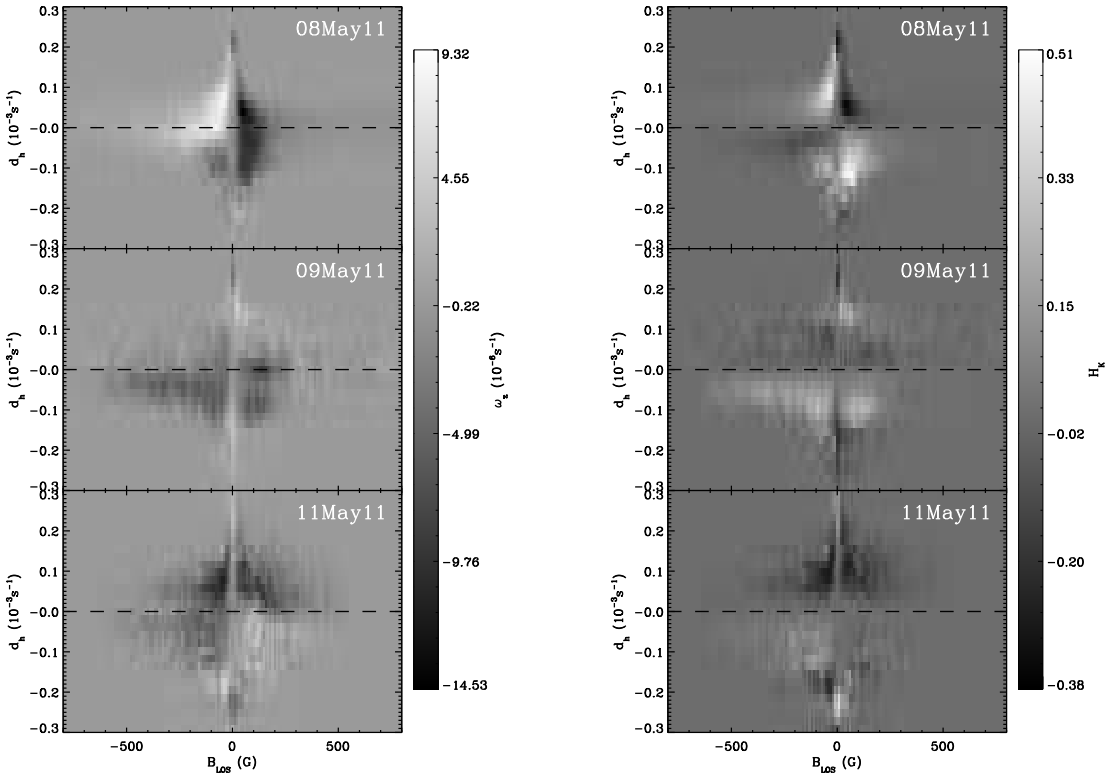

Figure 3.3: Vertical (z-component) vorticity, $\omega_z(d_h, B)$, and kinetic helicity, $H_k(d_h, B)$ (right panels), binned against LOS magnetic field, B (x-axis), and horizontal divergence, d_h (y-axis). The results here are calculated from LCT of granular motions imaged in HMI Doppler velocities, and are averages over the emerging flux region in the southern hemisphere on 2011 May 8 (top panels), 9 (middle panels), and 11 (bottom panels). See the text for further details.

the emerging flux region separately for the 3 dates are shown in Figure 3.3 wherein the results are based on LCT velocities derived using HMI Doppler velocities. It is to be noted that the signed averages $\omega_z(d_h, B)$ ($H_k(d_h, B)$) have cancellations and hence measure only the excess of one sign of rotation (either clock-wise (negative) or counter-clockwise (positive) rotation) over the other. In Paper I the dominance of one sign of $\omega_z(d_h, B)$ for flows around magnetised regions is explained to be due to the phenomenon of flux expulsion (Proctor & Weiss, 1982) which leads to magnetic flux occupying preferentially the inflow (negative d_h) locations.

3.4.1 Time evolution of vorticity-divergence relation

The emergence of magnetic flux as explained above starts on 2011 May 8 as observed on magnetograms in Figure 3.2. During its emergence, the vortical motions associated with the magnetised flows are found to be influenced by the emergence as seen in top panel in Figure 3.4. In Figure 3.3, the largest values of ω_z (H_k) are found in the positive divergence region for this emerging region. This diverging fluid is rotating in opposite directions during this emergence *i.e.,* the positive and negative fields are found to rotate in opposite directions (clockwise and counter-clockwise directions respectively) on 2011 May 8. This is speculated to occur due to transfer of magnetic helicity to the fluid motions from a highly twisted magnetic flux tube. This behaviour is found vanish on other two days.

3.4.2 Influence of emerging flux on vorticity

The results in Figure 3.3 show that, to a large extent, the sign of ω_z (H_k) is negative (positive) or clockwise rotation which is expected in southern hemisphere. Due to the prescence of emerging flux, ω_z shows a positive sign on the 3 dates. The positive sign of ω_z is found to be moving around from positive d_h to negative d_h and again to positive d_h depending on the movement of the emerging flux. This could be the effect of the emergence on the fluid motions where the emerging flux is changing the fluid physical pattern observed or could be due to the supergranular evolution (dying inflow that is replaced by the outflow of a new supergranule) can also contribute to the observed signatures.

As discussed in Paper I, in the absence of Coriolis and any other large-scale force, the flows are expected to have a roughly equal distribution of clockwise (negative) and counter-clockwise rotations, and hence a signed average of ω_z or H_k over the magnetic and divergence bins is expected to yield near-zero values due to cancellation among positive and negative vorticities. Earlier studies have shown the influence of Coriolis force on the supergranular-scale flows. Quiet-Sun areas devoid of significant magnetic field are captured in the central vertical area close to $|B| = 0$G in Figure 3.3. We take the average of ω_z within $|B| < 15$G, *i.e.*, a horizontal average over three magnetic bins of -10, 0, and 10 G in Figure 3.3, to determine

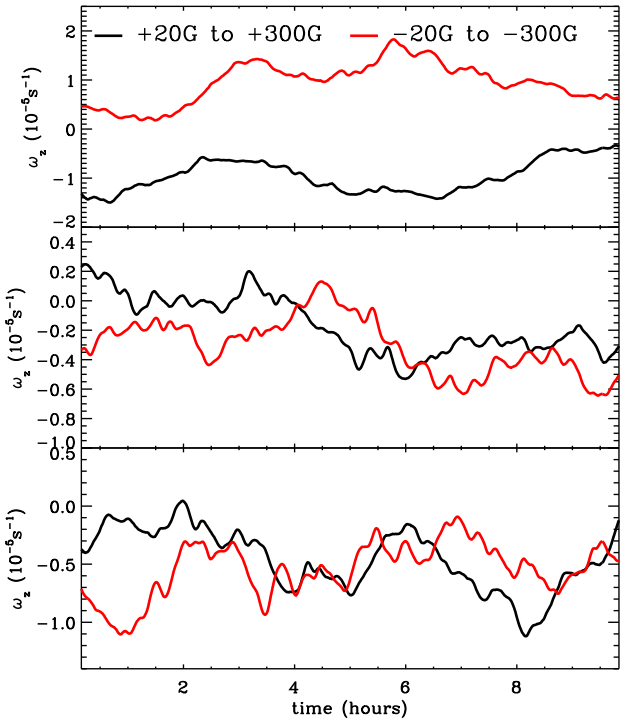

Figure 3.4: ω_z against time averaged over +20 to +300 G (black curve) and −20 to −300 G (red curve) derived from HMI Doppler velocities for 2011 May 8 (top panel), 9 (middle panel), and 11 (bottom panel). The start time for the three dates are different, $t = 0$ for 2011 May 8 corresponds to 4 hr, for 9 it is 8 hr, and 11 it is 2 hr.

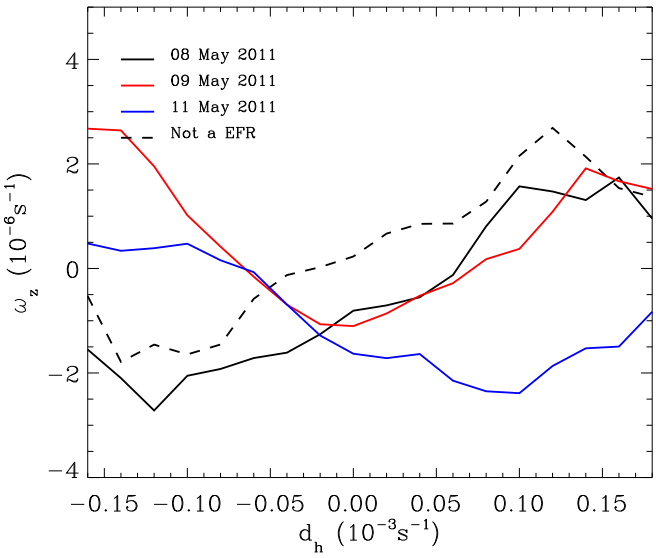

Figure 3.5: Averages over $|B| < 10G$ of vertical vorticities $\omega_z(d_h, B = 0)$ calculated from results shown in Figure 3.3 for 2011 May 8 (black), 9 (red), and 11 (blue). The figures shows signed ω_z against signed d_h. The dashed curve (black) is for a region without any flux emergence in the same latitude and longitude range as the observed data during emergence. (EFR in the figure indicates emerging flux region.)

$\omega_z^q(d_h) = \omega_z(d_h, B = 0)$ for the non-magnetic flows. In Paper I, for southern hemisphere for negative d_h, ω_z is negative and for positive d_h, ω_z is positive for quiet-Sun. This behaviour is again captured for 2011 May 8, but as for 2011 May 9, 11 dates this behaviour gets altered as shown in Figure 3.5. This could be the effect of transfer of helicity from the emerging flux to the fluid motions around it. To confirm this, a region in the same latitute and longitude range was selected where there was no flux emergence. It has similar behaviour as in 2011 May 8. The changes seen are 2011 May 9, and 11 can then be confirmed as after effects of flux emergence on fluid motions around the magnetic fields.

3.5 Summary

We have derived and analyzed horizontal fluid motions on the solar surface over the emerging flux region using LCT of convective granules imaged in

Doppler velocity by the HMI onboard *SDO*. We have studied the relationships between fluid divergence and vorticity. The main results obtained for the work done till now can be summarised as follows.

1. The correlations between vorticity and divergence is still seen in the emerging flux region. But their correlation is slightly altered by the emergence.

2. In the quiet-Sun deviod of any magnetic field the Coriolis effect seen in the vorticity - divergence relation and this relation gets affected due the flux emergence. This could be the effect of the transfer of helicity from the magnetic fields to the fluid motions around it.

3. During the evolution, the diverging fluids are found to rotate in opposite directions which is speculated to be due to the transfer of magnetic helicity to the fluid motions.

The transfer and redistribution of vorticities by magnetic fields implied by result (2) is the basic magnetohydrodynamic effect known from early laboratory experiments involving conducting liquid metals performed and expounded by Shercliff (1971). These results also give an insight that the emerging flux do have an inbuilt helicity as predicted by dynamo theories. Though whether this helicity of the flux tubes are inherent property of the emerging flux or acquired property of the flux tube during its rise through the convection zone cannot be told at this point. All that could be said is that the flux tubes do possess helicity during their emergence in the photosphere and is transfering a part of its helicity to the fluid motions around the flux tube. Further analysis has to be carried out in this regard to understand more on the transfer of helicity from fluid motions.

Part II

The effects of waves in lower chromospheric heating

Chapter 4

Wave dynamics of quiet-network of the Sun in lower atmosphere

4.1 Overview

[1]

p mode power suppression in photosphere is derived from the acoustic power of Doppler velocities from the Helioseismic and Magnetic Imager (HMI) onboard the *Solar Dynamics Observatory (SDO)*. The relation of p mode power suppression with chromospheric emissions in UV channels of the Atmospheric Imaging Assembly (AIA) onboard SDO is studied. Phase-shifts of the waves propagating from photosphere (we use continuum intensities for photospheric heights) to the chromospheric UV channels of 1600Å and 1700Å are derived. The influence of the line-of-sight, total magnetic field of SDO/HMI and the inclination of magnetic field derived from HMI/SDO vector magnetograms on p mode power suppression, the chromospheric emissions in UV channels, and on the phase-shifts of the waves are studied. The cut-off frequencies for the propagation of waves at different inclination angles of the field are calculated. The energy fluxes are derived from the phase-shifts and cut-off frequencies. These fluxes are compared with one another and earlier work.

[1] *The work presented in this chapter will be submitted for a refreed journal*

4.2 Introduction

The solar acoustic waves (p modes) are generated in the convection zone due to turbulence and they propagate in the solar interior (Goldreich & Kumar, 1990; Nordlund & Stein, 2001; Stein & Nordlund, 2001). Waves with frequencies greater than the acoustic cut-off frequency ($\nu_{ac} = \Gamma g/4\pi c = 5.3mHz$ for photosphere; $\Gamma = 5/3$ is the ratio of specific heats, $g = 274ms^{-2}$ is the gravitational acceleration, $c = 7kms^{-1}$ is the sound speed) pass through the photosphere in the absence of magnetic field and in isothermal conditions. Waves with frequencies less than the cut-off frequency are trapped inside the Sun. They leak to the solar atmosphere through their interaction with the magnetic structures on the Sun like sunspots, magnetic bright points, pores, plage regions and many more. The acoustic cut-off frequency then gets reduced ($\nu_{ac}^{B} = \nu_{ac} cos\theta$; where θ is the inclination of the magnetic field to the normal of the solar surface). These acoustic waves are thought to be a possible source of solar atmospheric heating. Hence, these waves have been studied over the years addressing the issues on how these waves are generated, how these waves propagate, do these waves carry sufficient energy, and importantly how the energy carried by these waves are dissipated. Sunspots waves are observed more prominently, as sunspot magnetic fields can be measured with more accuracy than the small-scale network fields. Recent results using TRACE data and simulations have proved that waves with frequencies greater than the cut-off frequencies donot carry sufficient energy to heat the solar atmosphere (Fossum & Carlsson, 2005a). On the other hand observations have confirmed that waves with frequencies less than the cut-off frequencies are observed in the higher solar atmosphere (De Pontieu et al., 2005, 2004; Jefferies et al., 2006a,b; McIntosh & Jefferies, 2006; Rajaguru et al., 2013). Bel & Leroy (1977) have theoretically shown that in the prescence of inclined fields the waves with frequencies less than the cut-off frequency travel through the inclined fields to higher solar atmosphere. Different categories of waves are observed in penumbra and umbra and their propagation through the solar atmosphere has been studied (Centeno et al., 2006; Felipe et al., 2010; Lites, 1984, 1988; Lites et al., 1982; Tziotziou et al., 2006). Theoretical simulations and modeling of sunspot waves have been carried

out over the years to understand the questions addressed earlier (Bogdan et al., 2003; Cally & Bogdan, 1997; Cally et al., 1994; Khomenko & Cally, 2012; Khomenko & Collados, 2008, 2009). Magnetic elements in the quiet-Sun are difficult measure as they are very dynamic. In the recent times, due to high-resolution and high cadence observations have enbled to observe quiet-Sun magnetic structures in more detail. Observations of these waves have been carried out in the small-scale fields too in the recent years (Chitta et al., 2012; De Pontieu et al., 2005, 2004; Finsterle et al., 2004a,b; Jefferies et al., 2006a; McIntosh & Jefferies, 2006; Rajaguru et al., 2013). In the quiet-network, through the small-scale network field, the waves with frequencies less than cut-off frequencies are observed to propagate to higher solar atmosphere through the so-called magnetoacoustic portals (Jefferies et al., 2006a,b). The inclination of the magnetic field used in Jefferies et al. (2006a) has been derived from MDI magnetogram data by extrapolation. The inclination of the field used in this paper has been derived using vector magnetic data from HMI. The vector fields of the magnetic field are derived using Milne-Eddington inversion by using the Very Fast Inversion of the Stokes Vector (VFISV; Borrero et al. (2011); see next section for more details).

All the proposed solar atmospheric heating mechanisms can be categorised into two main heating mechanisms: magnetic and non-magnetic (Narain & Ulmschneider, 1996; Ulmschneider & Musielak, 2003). In non-magnetic mechanism, acoustic waves are the source of dissipation of energy to higher solar atmospheric layers (Biermann, 1946; Ulmschneider, 1990). Magnetic heating is further classified into two sub-mechanisms, direct, and indirect magnetic heating. In direct heating, reconnection is the main process of dissipation of energy (Parker, 1991). While, in indirect magnetic heating, Joule heating through magnetic reconnection (Parker, 1988), dissipation of upward propagating magneto-acoustic waves (Alfvén, 1947; Schwarzschild, 1948), and high speed flows and jets play an important role in the dissipation of energy to the chromospheric layers (Narain & Ulmschneider, 1996; Ulmschneider & Musielak, 2003) : also see references therein.

Using multi-height observations, the propagtion of the waves and the direction of propagation can be obtained. By simultaneously measuring the acoustic power and hence the energy fluxes carried by these waves, one can understand whether these waves carry sufficient energy to heat the so-

lar atmosphere. Using SDO/HMI and AIA, we are able to observe Sun in multi-height from photosphere to lower chromosphere simultaneously. Along with the multi-height observations we have vector magnetic field information as well from HMI. We use this vector magnetic field information to determine the cut-off the frequencies. We derive phase-shifts of the waves propagating between photosphere (continuum intensities) and lower chromosphere (1600Å and 1700Å). Later with the spatial variation of acoustic power, we calculate energy flux using the cut-off of frequencies as well as phase-shifts. We compare the energy fluxes derived from these two methods and the results are presented in this paper. In this work, the interaction of p mode power supression coefficient, the chromospheric UV emissions, and the phase-shifts with magnetic fields and inclination of the fields are studied. This analysis could be carried out due to the continous observations done by Helioseismic and Magnetic Imager (HMI) and Atmospheric Imaging Assembly (AIA) onboard Solar Dynamics Observatory (SDO; Lemen et al. (2012); Schou et al. (2012)). In Section 2, data used for the analysis and the analysis techniques are discussed. In Section 3, the results of the analysis are discussed focussing mainly on the interaction of these with magnetic fields. In Section 4, a summary of the results are discussed.

4.3 Data and analysis

The data has been taken from the Helioseismic and Magnetic Imager (HMI) and Atmospheric Imaging Assembly (AIA) on-board Solar Dynamics Observatory (SDO). The observables taken from HMI are continuum intensities (I_c), Doppler velocity (v_d), photospheric line-of sight (LOS), and vector magnetograms (B_{LOS}, B_{tot}, respectively), and lower chromospheric UV emissions in the wavelength channels 1700 Å and 1600 Å (I_{uv1}, I_{uv2} respectively) are from AIA. We have studied quiet-sun regions (as shown by white dashed lines in the Figure (4.1) with separates the quiet-netwrok) around four active regions: NOAA11092, NOAA11161, NOAA11243, and NOAA11306 which cross the central meridian on 03 August 2010, 19 February 2011, 03 July 2011, and 02 October 2011, respectively for 14 hours (except NOAA11161 which is observed for 12 hours) starting from universal time 00:00. The line-of-sight observables from HMI have 45s cadence, and

vector magnetograms have a cadence of 720s and those from AIA have 24s cadence. Spatial resolution of the above data is $0.5''\ pix^{-1}$ covering an area of around $380 \times 380 Mm^2$ on the Sun. The magnetically sensitive line Fe I 6173.34 Å line is considered for the study of the photospheric physical quantities. The formation region of the line is in the range $0 - 300km$. The details about the line and its formation are discussed in Scherrer et al. (2012).

The temporal averages of B_{LOS} for the four active regions mentioned above are shown in Figure (4.1). The figure is saturated for between $\pm 200G$ to clearly see the small-scale magnetic network features. In Figure (4.1), the quiet-Sun region used for the analysis has been marked by white dashed lines. The area outside the regions consisting of sunspots, separated by white dashed lines, is considered as the quiet-Sun area for our analysis. It has to be noted that even though we call it quiet-Sun, it consists of kG field strength in a few localised small regions.

The temporal averages of I_{uv1} and I_{uv2} for the same four active regions used for the analysis are shown in Figure (4.2). In Figure (4.2) a lot of emissions is observed in the quiet-Sun which are we have tried to correlate with the power suppression in the photosphere. The average formation heights of I_{uv1} and I_{uv2} is derived to be around $360km$ and $430km$ respectively (Fossum & Carlsson, 2005b).

The field inclination γ is defined from the vector field maps B_x, B_y, and B_z as $\gamma = \tan^{-1}(B_z/B_h)$, where $B_h = \sqrt{B_x^2 + B_y^2}$. γ varies from -90°to +90°where $\mid \gamma \mid = 90°$ then the field is vertical and $\gamma = 0°$then the field is horizontal (Rajaguru et al., 2013; Schunker & Braun, 2011). It should be noted here that γ is defined w.r.t the tangent of the surface, while θ in the cut-off frequency is defined w.r.t. to the normal of the surface. We can get θ from γ as $\theta = 90 - |\gamma|$. The total field strength is defined as $B_{tot} = \sqrt{B_x^2 + B_y^2 + B_z^2}$.

From v_d, spatial variation of p mode power is derived using a pixel-wise Fourier power spectra in the frequency range 2-10 mHz. These power maps are normalised by quiet-Sun average (as marked by dashed line in Figure

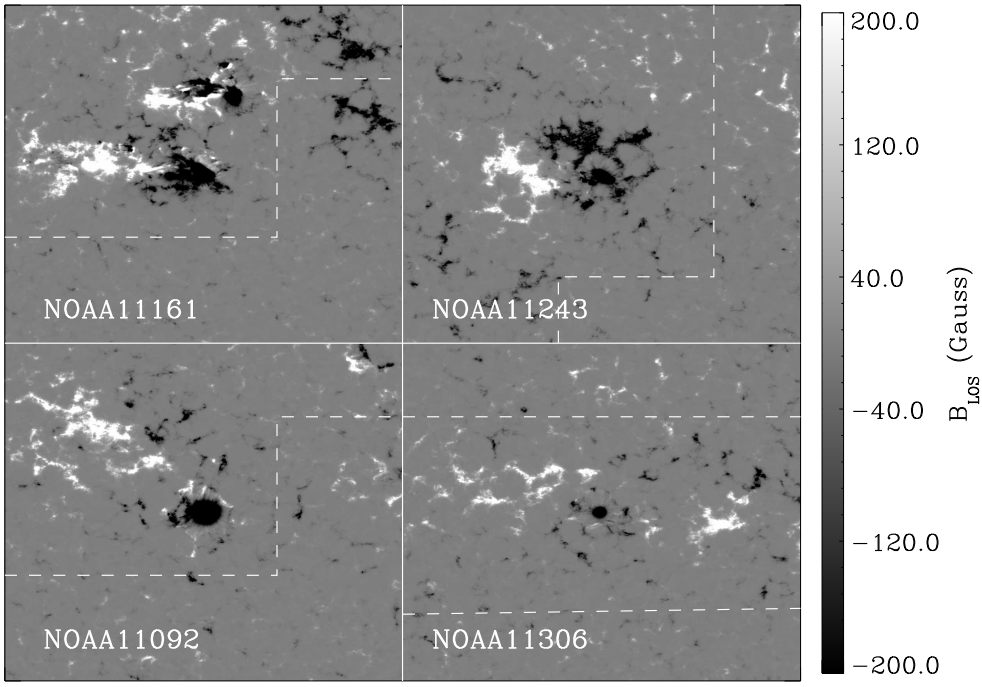

Figure 4.1: The averaged B_{LOS} for the four active regions saturated between $\pm 200G$ to make the small-scale network magnetic features visible. The white dashed lines separates the regions containg the sunspots and the quiet-network fields. In our analysis, we have used the regions outside those containg sunspots.

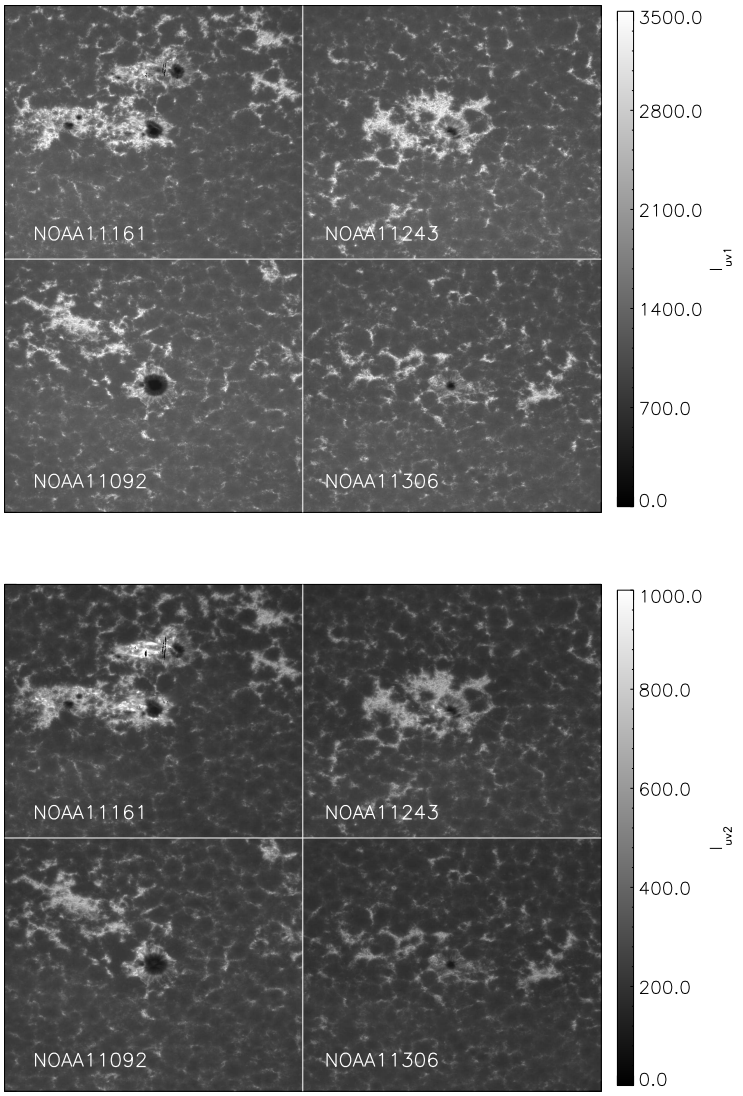

Figure 4.2: The top panel shows the temporal averaged I_{uv1} and I_{uv2} is shown in the bottom panel for the four active regions mentioned earlier.

4.1). The power suppression coefficient α is calculated as below

$$\alpha = 1 - \frac{p(x, y, \nu)}{p_q(\nu)}, \tag{4.1}$$

where $p(x, y, \nu)$ is the spatial power map as a function of frequency, and $p_q(\nu)$ is the quiet-sun power at each frequency (Bogdan et al., 1993). Bogdan et al. (1993) defines this term as so-called absorption coefficient for different frequencies. Since we are calculating this coefficient at each and every pixel, we term it as power suppression coefficient. Since less amount of power at certain pixel need not just mean that power is getting absorbed at certain pixel. The power could have been absorbed by the pixels surrounding it and hence the energy would not have reached the area of interest. The spatial power suppression coefficient maps are shown in Figure 4.3 and are averaged over frequencies 2-5mHz. When $\alpha > 0$ then it implies that power is getting suppressed and when $\alpha < 0$ then the waves are thought to be reflected back to the photosphere (Khomenko & Collados, 2009) and has been attributed to acoustic power halo.

The phase-shifts of the waves propagating between two heights is derived from,

$$\phi = 180 \ \tan^{-1}[\boldsymbol{I}(z_1, \nu)\boldsymbol{I}^*(z_2, \nu)]/\pi, \tag{4.2}$$

where, $\boldsymbol{I}$ is the Fourier transform of I_c at the two heights z_1 and z_2 (Rijs et al., 2016). Here, the two heights are the photosphere and lower chromosphere. We have used I_c for photosphere and I_{uv1} and I_{uv2} for the lower chromospheric heights. Using the derived ϕ we calculate the phase travel times of the waves from photosphere to chromosphere as, $\triangle t_p = T\ \phi$, where, T is the wave period. Here, positive ϕ ($\triangle t_p$) would imply that the waves are propagating upwards. Negative ϕ ($\triangle t_p$) would imply the propagation of waves is in opposite direction.

The spatial distribution of energy fluxes are estimated for both I_{uv1} and I_{uv2} chromospheric emissions from v_d. The energy flux can derived as,

$$F(x, y, \nu) = p(x, y, \nu)\ v_g(x, y, \nu)\ \rho \tag{4.3}$$

where, ρ is the density of plasma at a particular height, and $v_g(x, y, \nu)$ is the group velocity of the waves (Canfield & Musman, 1973). ρ is taken

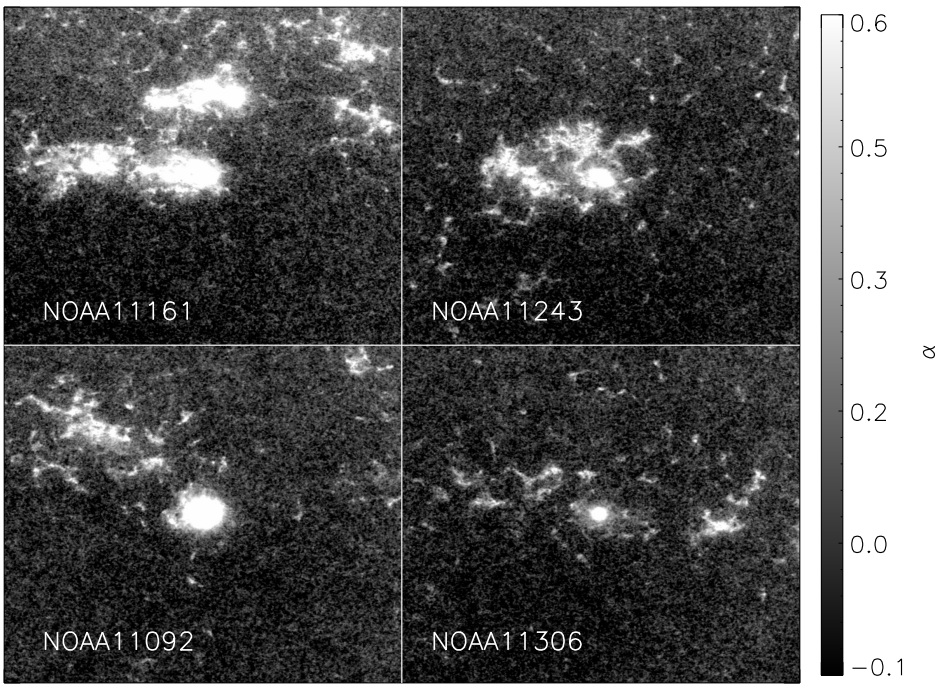

Figure 4.3: The maps shows the spatial power suppression coefficient for the four active regions. In the figure, α is averaged over 2-5mHz. The power suppression coefficients are derived from Doppler velocities.

from VAL C model atmosphere (Vernazza et al., 1981) for average formation heights of I_{uv1} and I_{uv2}. $\rho = 2.334 \times 10^{-8} gcm^{-3}$ for I_{uv1} and $\rho = 9.327 \times 10^{-9} gcm^{-3}$ for I_{uv2}. We calculate the group velocity of waves in two different ways. The first method is from $\triangle t_p$, where we calculate v_g^{ϕ} (v_g calculated from $\triangle t_p$) using, $v_g^{\phi}(x, y, \nu) = \frac{c^2 \ \triangle t_p(x,y,\nu)}{\triangle z}$ where, $\triangle z$ is average formation height from the photosphere (Jefferies et al., 2006a). The second method is from ν_{ac}^{B}, we calculate v_g^{c} (v_g calculated from ν_{ac}^{B}) as $v_g^c(x, y, \nu) = c \sqrt{1 - \left(\frac{\nu_{ac}^{B}(x,y)}{\nu}\right)^2}$ (Bello González et al., 2009).

4.4 Results

In this study, we have

1. Calculated the phase-shifts of waves travelling between photosphere (I_c) and lower chromosphere (I_{uv1} and I_{uv2}).

2. Looked into the variation of α, the derived phase-shifts, and the UV emissions I_{uv1} and I_{uv2} with B_{LOS}, B_{tot}, and $\mid \gamma \mid$.

3. Tried to see how the power suppression is correlated to these emissions in the UV channels.

4. Estimated energy fluxes at I_{uv1} and I_{uv2} average formation heights from phase-shifts as well as from the cut-off frequencies.

5. Compared the energy flxes derived from these methods.

To do this, we try to first see the dependence of α, I_{uv1}, I_{uv2}, $\triangle t_p$ and B and γ by calculating their averages over choosen small intervals (bin sizes) in B_{LOS}, B_{tot}, ν, and $|\gamma|$: 30G for B_{LOS}, and B_{tot}, 4°for $|\gamma|$, and 0.25mHz for ν.

4.4.1 Influence of B_{LOS}, B_{tot}, γ on I_{uv1} and I_{uv2}

The variation of I_{uv1} and I_{uv2} with B_{LOS}, B_{tot}, and $|\gamma|$ is as shown in Figure (4.4). The top panels in the Figure (4.4) shows for I_{uv1} and the bottom panels for I_{uv2}. The left panels of Figure (4.4) shows variation

of I_{uv1} and I_{uv2} with B_{LOS}, middle panels shows I_{uv1} and I_{uv2} with B_{tot} and right panels shows the variation of I_{uv1} and I_{uv2} with $|\gamma|$. I_{uv1} and I_{uv2} shows a linear increase with B_{LOS} and B_{tot} up to 300G, saturates a little and decreases slightly up to 1000G, and a sharp decline is seen beyond 1000G. Loukitcheva et al. (2009a,b), show linear variation of chromospheric emissions with B_{LOS} up to 200G. These authors have concluded that heating in quiet-Sun map well with the underlying photospheric magnetic fields. In our analysis too, we see this correlation in I_{uv1} and I_{uv2} with B_{LOS}. Since HMI provides vector magnetic fields, we carried out this analysis for B_{tot} and got similar results. This correlation of I_{uv1} and I_{uv2} with B_{LOS} and B_{tot} partly confirms the theoretical predictions that waves with frequencies less that ν_{ac} propagate to higher solar atmosphere through their interaction with magnetic fields.

I_{uv1} and I_{uv2} for 0°- 20°range doesn't show any variation with $|\gamma|$, from 20°- 70°increases linearly with $|\gamma|$, and saturates beyond it. Schunker & Cally (2006) in their modeling find that acoustic energy is maximum around 20°-30°from the normal to the surface. Our results are in agreement with these results, the maximum is found to be around 70°from the horizontal, which implies that in our results, the maximum is around 20° from the normal. We also see that the heating of chromosphere can be correlated to the presence of inclined fields. This further corroborates that the wave propagation can happen through inclined fields.

For the quiet-Sun regions around active regions NOAA11306, I_{uv1} and I_{uv2} values are slightly less than the other active regions for B_{tot} and $|\gamma|$ binning. The red curves in the Figure (4.4) are derived for the regions around active region NOAA11306. The black curves for B_{tot} and $|\gamma|$ of I_{uv1} and I_{uv2} are the averages for the regions around other three active regions. This variation in regions around active region NOAA11306 is still not completely understood, but it thought to be due to some miscalculation in vector field measurements.

4.4.2 Influence of B_{LOS}, B_{tot}, γ on α

An average of α is taken over 2-5mHz, 5-7mHz, 7-9mHz, and 9-10mHz frequency range and the variation of α, against B_{LOS}, B_{tot}, and $|\gamma|$ over

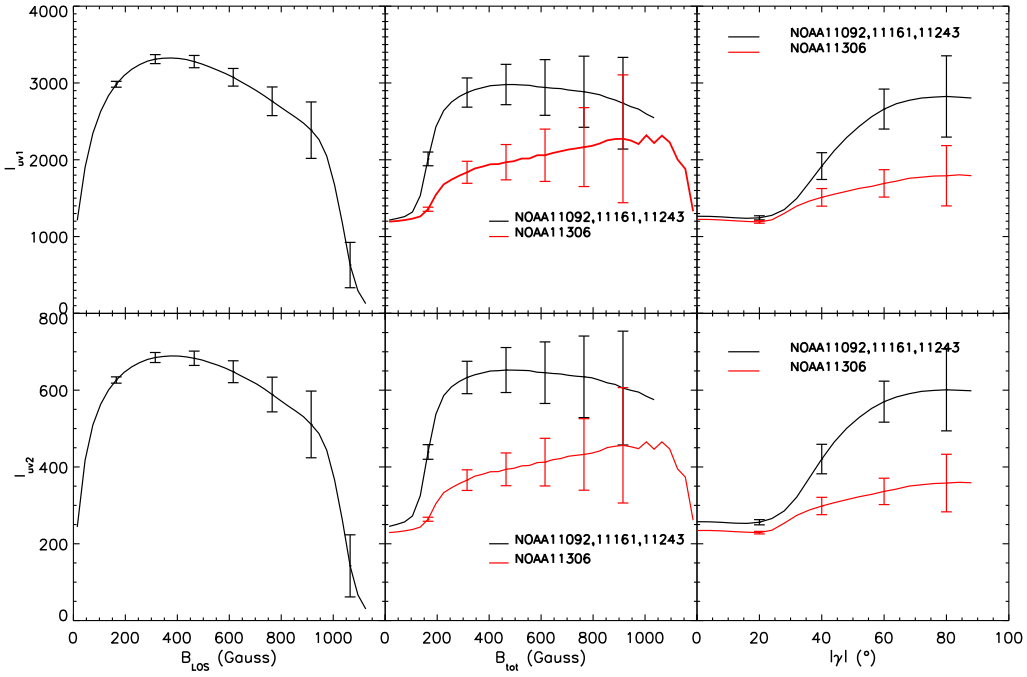

Figure 4.4: The top panels shows the variation of I_{uv1} with B_{LOS}, B_{tot}, and $|\gamma|$ in the quiet-network fields. The bottom panels shows the same but for I_{uv2}. The red curves in the B_{tot} and $|\gamma|$ shows that the variation of the same quantities but for the regions around sunspot NOAA11306. We see a slight decrease in the values of I_{uv1} and I_{uv2} for this region.

these frequency range are shown in Figure (4.5). The top panels in Figure (4.5) are for α in frequency range 2-5mHz. Also, the I_{uv1} emissions are overplotted in red to compare the variation of α in the frequency range 2-5mHz and I_{uv1} with the physical parameters above. The variation of α in frequency range 2-5mHz and I_{uv1} with the physical variables is seem to correlate very well. The same behaviour is seen with I_{uv2} (not shown in the figure). α in the frequency range 2-5mHz is positive which implies power is getting supressed. This implies that the locations where the power is getting suppressed in photosphere is mostly in the presence of inclined magnetic fields. These locations also found to be areas in the chromosphere where emissions are seen. The excess energy that is seen in chromosphere could have the source in the photosphere at the magnetic footpoints. The waves escaping from the photosphere could then have absorbed the energy in photosphere due it's interaction with magnetic fields. These results are in agreement with the previous results (Bel & Leroy, 1977; Rajaguru et al., 2007, 2010).

The bottom panels of Figure (4.5) are for α in the frequency ranges 5-10mHz. The left panels shows the variation of α with B_{LOS}, the middle panels with B_{tot} and the right panels with $|\gamma|$. α in the frequency range 5-7mHz are found to have negative values below 200G in B_{LOS}, below 400G in B_{tot}, and below 50° in $|\gamma|$. This reduction in α is the effect of the so-called acoustic halo. Rajaguru et al. (2013) has explained this as the waves propagating are getting reflected causing these canopies. Further, these observational features agree with the theory and simulations carried by Khomenko & Collados (2009). We are not focusing further on this as we are mainly interested in the 2-5mHz frequency range for this work.

4.4.3 Influence of B_{LOS}, B_{tot}, γ on $\triangle t_p$

The phase shifts $\triangle t_p$ shows fluctuations in space and frequency. Hence, these have been averaged over the frequency band 2-5mHz to study the behaviour of these phase shifts with B, B_{tot}, and $|\gamma|$. The $\triangle t_p$ between I_c and I_{uv1} is denoted as $\triangle t_{p_1}$, and between I_c and I_{uv2} as $\triangle t_{p_2}$. The variation of $\triangle t_{p_1}$, and $\triangle t_{p_2}$ in the frequency range 2-5mHz with B_{LOS}, B_{tot}, and $|\gamma|$ are in Figure (4.6). The top panels shows the variation of $\triangle t_{p_1}$ in the

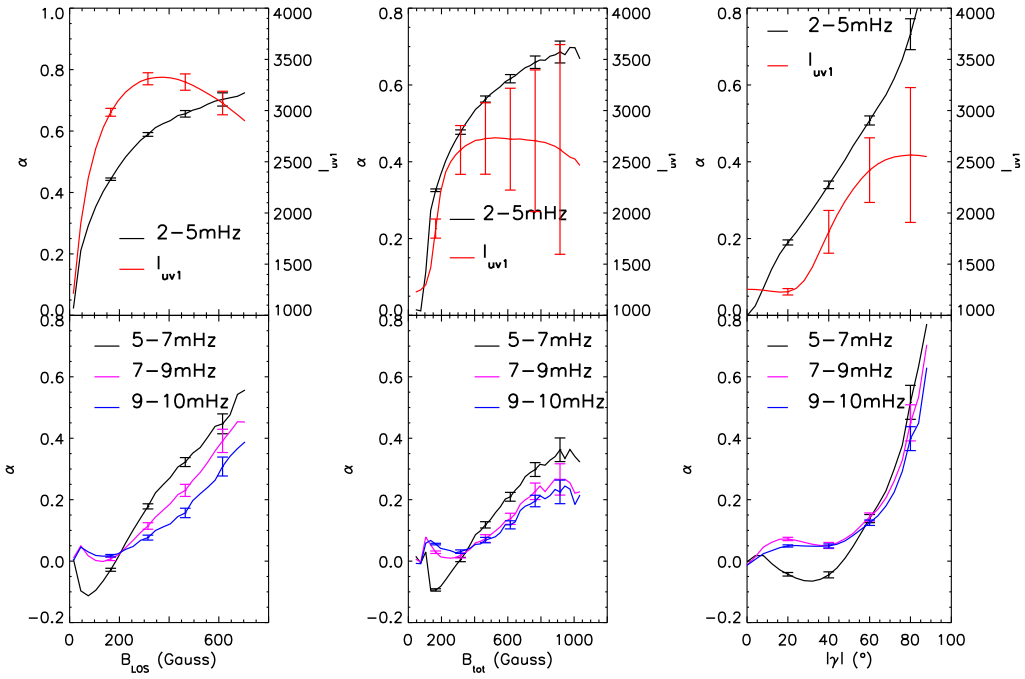

Figure 4.5: The top panels shows the variation of α in 2-5 mHz range with B_{LOS}, B_{tot}, and $|\gamma|$. I_{uv1} are over-plotted to show the correlation between α in the frequency range 2-5 mHz with I_{uv1}. The bottom panels shows the variation of α in the frequency ranges 5-7, 7-9, and 9-10mHz (black, pink, and blue curves, respectively) with the same parameters as the top panels.

frequency range 2-5mHz with the mentioned above physical parameters, and bottom panels for the variation of $\triangle t_{p_2}$ in the frequency range 2-5mHz. The left panels shows the variation of $\triangle t_{p_1}$, and $\triangle t_{p_2}$ in the frequency range 2-5mHz with B_{LOS}, the middle panels with B_{tot}, and right panels with $|\gamma|$. The I_{uv1} and I_{uv2} are overplotted over $\triangle t_{p_1}$, and $\triangle t_{p_2}$ in the frequency range 2-5mHz to compare these observables. We see that $\triangle t_{p_1}$, and $\triangle t_{p_2}$ in the frequency range 2-5mHz variation is similar to what we see in the I_{uv1} and I_{uv2}. Furthermore, we have considered only those regions with positive $\triangle t_p$ since we are only interested in upward propagating waves for this work. This implies that the waves are travelling in the presence of inclined magnetic field. Also, the locations of chromospheric emissions are mapping well with the locations where $\triangle t_p$. This means that the waves in the frequency range 2-5mHz have the potential to carry energy from photosphere to chromosphere. In other words, the propagation of p mode waves happens in the magnetised regions. These results are in agreement with analysis carried out by Rajaguru et al. (2007, 2010); Rijs et al. (2016).

4.4.4 Energy flux

The energy flux derived from v_g^c is denoted as F^c and those from v_g^ϕ are denoted as F^ϕ. The energy flux calculated between I_c and I_{uv1} as F^{c_1} and F^{ϕ_1} and the flux between I_c and I_{uv2} as F^{c_2} and F^{ϕ_2}. The spatial maps of F^{c_1}, F^{ϕ_1}, F^{c_2}, and F^{ϕ_2} in the frequency range 2-5mHz (avearge in this frequency range) are shown in Figure (4.7). The top panels of Figure (4.7) shows the spatial maps of fluxes derived from cut-off frequencies, while bottom panels shows for phase travel times. The left panels are for F^{c_2} and F^{ϕ_2} while the right panels are for F^{c_1} and F^{ϕ_1}.

To calculate F from Equation (4.3), p from v_d, p^v, is used in usual analysis (De Moortel & Rosner, 2007; Jefferies et al., 2006a). The p^v is found to have excess area of power suppression around the magnetic pixels due to projection effects. To remove these effetcs, we have done a small correction to the p used in Equation (4.3). We have used the p from continuum intensities, p^I, to remove the area around the magnetic pixels due to projection effects. An average of p^I for $B_{tot} < |150|G$ is taken and we call it as p_q^I. The p for all the other regions with $B_{tot} > |150|G$, p_b^I, is divided by p_q^I ,i.e.,

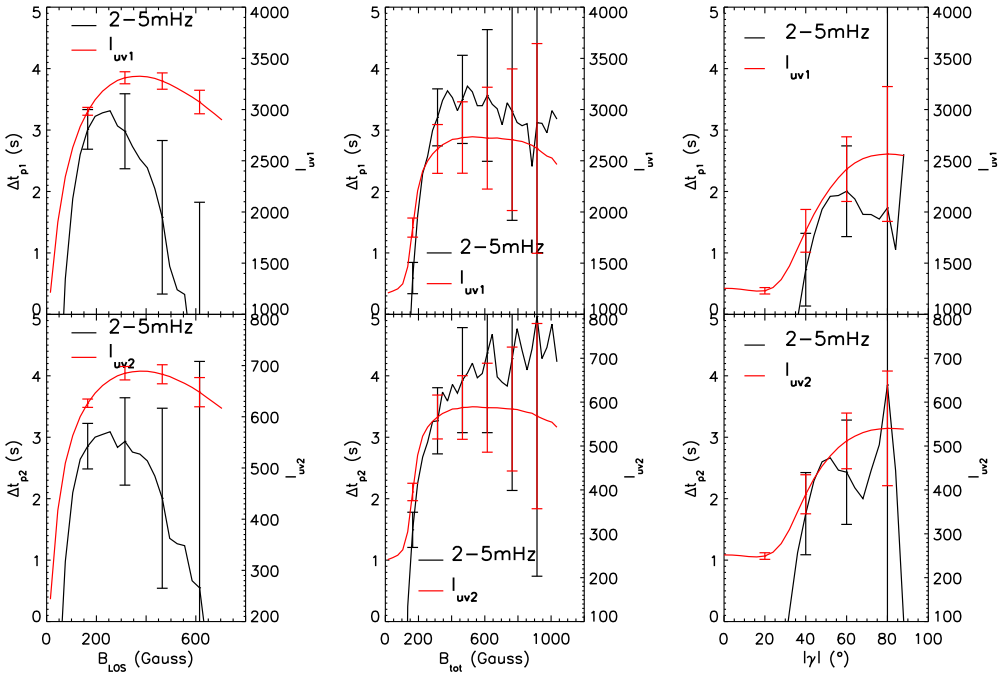

Figure 4.6: The top panels shows variation of $\triangle t_{p_1}$ along the B_{LOS}, B_{tot}, and $|\gamma|$ in 2-5mHz range. Also, I_{uv1} is plotted in red curves to see the correlation of $\triangle t_{p_1}$ with I_{uv1}. The bottom panels shows tha variation of $\triangle t_{p_2}$ along the same parameters as the top panels and I_{uv2} is overplotted in red.

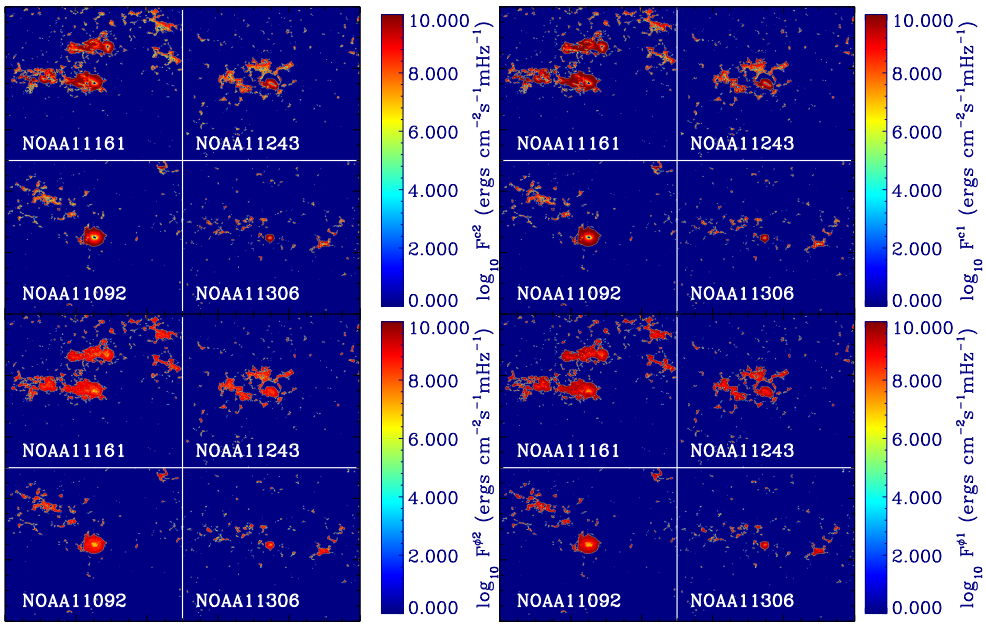

Figure 4.7: The left panels of the figure shows the F^{ϕ_2} and F^{c_2} derived from phase-shifts and cut-off frequencies respectively (top panel from cut-off frequencies and bottom panel from phase-shifts) between I_c and I_{uv2} in the 2-5mHz frequency range. The right panels in the figure are same as left but for fluxes (F^{ϕ_1} and F^{c_1}) between I_c and I_{uv1}. The fluxes in the regions where $|B_{tot}| > 150$ G are only shown in the above figure. The background, hence is dark blue as these regions have $|B_{tot}| < 150$ G. Also, the fluxes are in logarithm scale.

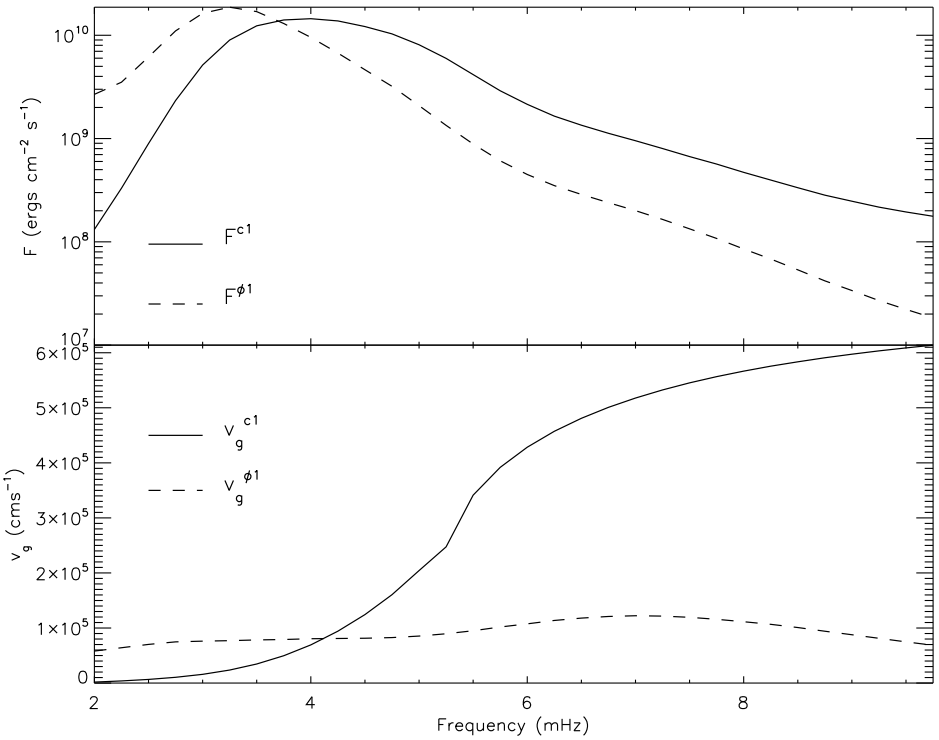

Figure 4.8: The top panel of the figure shows a plot of F^{ϕ_1} and F^{c_1} plotted against frequency. The ordinate of the top panel is in log scale. The bottom panel shows a plot of $v_g^{\phi_1}$ and $v_g^{c_1}$ against frequency. The solid curves are for the flux and velocity derived from cut-off frequencies, while the dashed curves are the flux and velocity derived from phase-shifts.

$f = \frac{p_b^I}{p_q^I}$, where f is defined as the correction factor. We now take an avearge of p^v, p_q^v, in regions with $B_{tot} < |150|G$. The final corrected power, p^c is given by, $p^c = f \times p_q^v$. We use p^c in Equation (4.3) instead of p. Also, while calculating F^c and F^ϕ we have used a threshold in B_{tot} by considering only those regions field strengths greater than $150G$. This is done to remove any background effetcs seen in the data. Further, for F^ϕ we have considered only the regions with positive $\triangle t_p$ as we are interested only in the upward propagating waves. All these corrections are done at every frequency step.

We first compare $v_g^{c_1}$ and $v_g^{\phi_1}$, and we find that their behaviour with the frequency is different from one another. $v_g^{\phi_1}$ is mostly constant with frequency and $v_g^{c_1}$ increaces rapidly for upto $6mHz$ and starts to saturate after that. The results are shown in the bottom panels of Figure 4.8. Similar

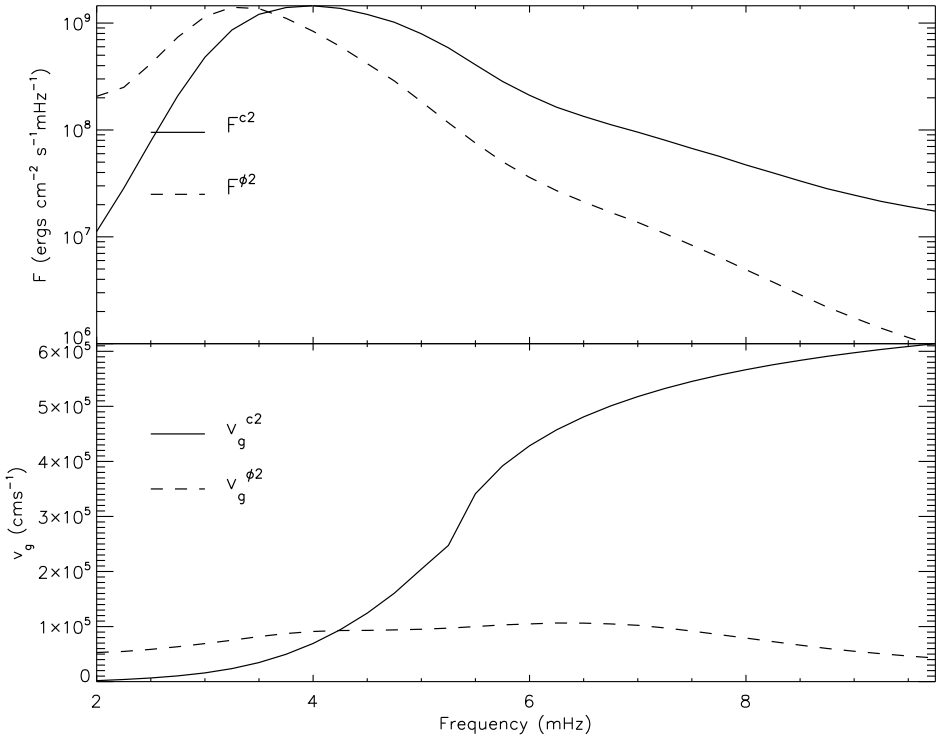

Figure 4.9: Same as Figure (4.8) but for fluxes F^{ϕ_2} and F^{c_2} and velocities $v_g^{\phi_2}$ and $v_g^{c_2}$

behaviour of $v_g^{c_2}$ and $v_g^{\phi_2}$ with frequency is seen and the results of these are shown in bottom panels of Figure 4.9.

We compare the fluxes F^{c_1} and F^{ϕ_1} as well as group velocities $v_g^{c_1}$ and $v_g^{\phi_1}$ (v_g calculated between I_c and I_{uv1}). The results are plotted in Figure (4.8). The top panel of Figure (4.8) shows variation of F against frequency while the bottom panel shows variation of v_g against frequency. The ordinate of top panel is in log-scale. F^{c_1} peaks at 3.75mHz, while F^{ϕ_1} peaks at 3.25mHz. The raise and fall of F^{c_1} and F^{ϕ_1} are very similar. The variation of F^{c_2} and F^{ϕ_2} against frequency is also similar as shown in Figure (4.9). F^{c_2} peaks at 4mHz, while F^{ϕ_2} peaks at 3.25mHz. It is clearly seen Figures 4.8, 4.9 that waves with frequency less than ν_{ac} are seen in lower solar chromosphere which confirms that waves with frequencies less than ν_{ac} travel through higher atmospheric layers through inclined fields. The integrated energy fluxes at I_{uv1} and I_{uv2} heights integrated over all frequencies is found to be $\sim 6.5\times10^6 ergscm^{-2}s^{-1}$ and $\sim 3.1\times10^6 ergscm^{-2}s^{-1}$ derived from ν_{ac}^B, and $\sim 6\times10^6 ergscm^{-2}s^{-1}$ and $\sim 2.3\times10^6 ergscm^{-2}s^{-1}$ derived from $\triangle t_p$. Also, we find the integrated fluxes intergrated in the frequency range 2-5mHz at I_{uv1} and I_{uv2} heights is $\sim 5\times10^6 ergscm^{-2}s^{-1}$ and $\sim 2.4\times10^6 ergscm^{-2}s^{-1}$ derived from ν_{ac}^B, and $\sim 5.7\times10^6 ergscm^{-2}s^{-1}$ and $\sim 2.2\times10^6 ergscm^{-2}s^{-1}$ derived from $\triangle t_p$. Further, we find the integrated fluxes integrated over the frequency range 5-10mHz for the same heights as above and is found to be $\sim 1.4\times10^6 ergscm^{-2}s^{-1}$ and $\sim 7\times10^5 ergscm^{-2}s^{-1}$ derived from ν_{ac}^B, and $\sim 3.1\times10^5 ergscm^{-2}s^{-1}$ and $\sim 1.2\times10^5 ergscm^{-2}s^{-1}$ derived from $\triangle t_p$. Chromospheric radiative losses as found to be around $1-2\times10^6 ergcm^{-2}s^{-1}$ (Wunnenberg et al., 2002) for the quiet-network. High concentrations of F are seen in the regions of magnetic field (Figure 4.7). This further confirms that magnetic field is needed for the transport of the energy from photosphere to higher solar atmosphere. Also, our analysis is in agreement with Jefferies et al. (2006a,b) that in the prescence of inclined fields magnetoacoustic portals are responsible for the leakage of energy from photosphere to chromosphere. Jefferies et al. (2006a) have found energy flux from $\triangle t_p$ of the order $1.4\times10^6 ergcm^{-2}s^{-1}$ in 2-5mHz. Bello González et al. (2010) have energy flux from ν_{ac}^B around $1.73-2.06\times10^6 ergcm^{-2}s^{-1}$ in 2-5mHz. In our analysis, we have selected only those areas with $B_{tot} > |150|G$ to improve the statistics of the energy flux. This has need helped to get slightly

higher values of integrated F than the previous studies. Eventhough the order of the fluxes are same, the values are slightly higher. We considered this analysis technique keeping in mind that the waves propagate to higher atmosphere through the inclined magnetic fields. We speculate that while integrating the enenrgy fluxes, considering the fluxes in the non-magnetic regions are reducing the fluxes that is actually propagating to the higher solar atmosphere.

If we look into the energy fluxes at I_{uv1} and I_{uv2} heights, we see that energy is decreasing from I_{uv1} to I_{uv2} heights. This is the signature of the dissipation of energy of these waves while it is propagating from photosphere to chromosphere (Fontenla et al., 1993). So, in this work we see the correlation between p mode power suppression, the propagation of these waves, the energy carried by these waves, and most importantly the diddipation of energy due to these waves.

4.5 Conclusion

In this work, we have derived the energy fluxes at lower chromospheric UV emission bands I_{uv1} and I_{uv2}. We have found some interesting results from this analysis which are as follows:

1. We find a tighter correlation between p mode power suppression and the inclined magnetic fields as well as chromospheric emissions in UV bands and magnetic fields. This would imply that the locations of power suppression are the locations where the magnetic fields are present and are the locations where chromospheric emissions are found. This confirms the theoretical studies stating that inclined fields are responsible for the transport of energy fluxes. But this alone is not sufficient to prove the propagation of these waves.

2. The travel phase-times between photosphere and lower chromosphere are found to be correlated with each other. This means that the propagation of p mode waves from photosphere to lower chromosphere is observed. This propagation of waves further confirms the theoretical consideration of chromospheric heating with waves in the prescence of inclined fields.

3. The energy fluxes derived are found to be $\sim 5 \times 10^6 ergscm^{-2}s^{-1}$ and $\sim 2.4 \times 10^6 ergscm^{-2}s^{-1}$ derived from ν_{ac}^B, and $\sim 5.7 \times 10^6 ergscm^{-2}s^{-1}$ and $\sim 2.2 \times 10^6 ergscm^{-2}s^{-1}$ derived from $\triangle t_p$ for the chromospheric heights I_{uv1} and I_{uv2}. These are comparable to the chromospheric radiative losses for the chromosphere in the quiet-Sun. This implies that the waves carry sufficient energy to heat the lower chromosphere.

4. Eventhough the energy carried by these waves are more than sufficient to heat the lower chromosphere, we need to see the dissipation of energy of these waves in chromosphere. For this, multi-height data has to be considered and the decrease in energy of these waves at different heights are to be seen. In our analysis, we have carried out this at two different heights and have found that the energy of these waves is decreasing as the waves propagate to higher atmosphere. This confirms that these are capable of heating the lower chromosphere.

In our analysis, we have confirmed that the energy carried by the p mode waves are sufficient to heat the lower chromospheric heights. We have also seen the dissipation of energy of these waves as they move higher in the solar atmosphere. This dissipation of energy in this work was carried at two different heights in lower chromosphere. If we carry out this analysis at different heights in the solar atmosphere, one could see how the energy is dissipated with height and also with further confirm the energy dissipation of these waves as they propagate higher.

Chapter 5

Conclusions

5.1 Summary

In Chapter 1, a basic introduction for the background of this work is given with an importance on flows and waves on the Sun. The thesis is then divided into two parts: Part I deals with interactions between vortex flows and small-scale magnetic field and Part II deals with the effects of waves in chromospheric heating. The part I of the thesis aims at studying the interaction of fluid helicity and current helicity with the magnetic field. This interaction between fluid motions and magnetic fields is of importance in understanding the nature of fluid turbulence and the associated dynamo-sustaining state of near-surface convection (Brandenburg & Schmitt, 1998). These interactions between kinetic and magnetic helicities play fundamental roles in magnetic field generation (or dynamo action) as well as in the magneto-hydrodynamical evolution of the fluid and magnetic fields (Brandenburg & Subramanian, 2005; Parker, 1955). The part II of the thesis aims at the evolution of energy fluxes carried by the waves at different heights. Fontenla et al. (1993) states that energy fluxes of p modes decreasing with increasing height from the photosphere indicate that p modes are dissipating energy more than that is generated.

In chapter 2, the horizontal fluid motions are studied and some of the significant results are discussed as follows. The correlations between the vorticity and divergence of non-magnetic flows at the supergranular-scale have the dominant hemispheric sign pattern brought about by the action of

the Coriolis force. For magnetised flows, the sign pattern corresponding to the inflows dominates over the whole divergence field, *i.e.*, even the outflow regions (positive divergence, interiors of supergranules) exhibit the rotations expected from the action of the Coriolis force acting on inflows. In other words, for magnetised flows the dominant sign pattern is negative helicity H_k (positive ω_z) in the north and positive helicity H_k (negative ω_z) in the south. We have identified and attributed this to the mechanism of transfer of vorticity from network inflow regions to interiors of supergranules by the magnetic connectivity or by the horizontal component of magnetic field. The excess of inflow vorticities over those of outflows increases dramatically for magnetised flows. This excess of inflow vorticity has been identified as due to the preferred inflow locations of the magnetic fields resulting from the convective flux expulsion mechanism. The contributions of intrinsically larger rotations of inflows around stronger fields there due to thermal causes, however, can also play a role in the above asymmetries between outflow and inflow rotations. Regarding the absolute magnitudes of vorticities, it has been found that non-magnetic flows have the largest values. As a function of magnetic field strengths, as observed by HMI, the magnitudes of absolute vorticities decrease almost exponentially, causing the magnetic suppression of flows due to Lorentz forces.

In Chapter 2, we note that the dominance of negative kinetic helicity in the north, and hence the expected same sign for magnetic helicity, indicate a positive α-effect in the north in contrast to that required for explaining the observed butterfly diagram of large-scale active regions. As referred to earlier, more detailed analyses of the distribution of kinetic helicity, its interactions with the magnetic field, its spatio-temporal spectra, and their relations to various other local and global properties of solar magnetic fields are necessary to make progress toward devising observational diagnostics of possible dynamo actions happening in the near-surface layers. We note that continuous wide field of view observations of higher spatial resolution to resolve sub-granular scale flows and magnetic fields than provided by HMI/*SDO* is important to address such details. We believe that the kind of analyses undertaken here as applied to magnetic regions in different dynamical states such as emerging flux regions, decaying active regions, and those before, during, and after significant atmospheric activity such as eruptions

or flares, would aid in understanding the interactions between fluid and magnetic helicities, their evolution, exchange, and transport upwards in the atmosphere.

In Chapter 3, from the derived horizontal fluid motions, the following are some important points to ponder. The correlations between vorticity and divergence is still seen in the emerging flux region. But their correlation is slightly altered by the emergence. In the quiet-Sun devoid of any magnetic field the Coriolis effect seen in the vorticity - divergence relation and this relation gets affected due to the flux emergence. This alteration in the relationship between vorticity-divergence could be the result of the transfer of helicity from the magnetic fields to the fluid motions around it. The transfer and redistribution of vorticities by magnetic fields implied by the above result is the basic magnetohydrodynamic effect known from early laboratory experiments involving conducting liquid metals performed and expounded by Shercliff (1971). These results also give an insight that the emerging flux does have an inbuilt helicity as predicted by dynamo theories. Though whether this helicity of the flux tubes is inherent property of the emerging flux or acquired property of the flux tube during its rise through the convection zone cannot be told at this point. All that could be said is that the flux tubes do possess helicity during their emergence in the photosphere. Further analysis has to be carried out in this regard to understand more on the transfer of helicity from fluid motions.

In Chapter 4, the power suppression of p mode waves in photosphere is related to the emissions in the chromosphere in UV bands. We find a tighter correlation between p mode power suppression and the i nclined magnetic fields as well as chromospheric emissions in UV bands and magnetic fields. This correlation would imply that the locations of power suppression are the sites where the magnetic fields are present and are the places where chromospheric emissions are found. This correlation confirms the theoretical studies stating that inclined fields are responsible for the transport of energy fluxes. But this alone is not sufficient to prove the propagation of these waves. The travel phase-times between the photosphere and lower chromosphere are found to be correlated with each other. This correspondence means that the propagation of p mode waves from the photosphere to lower chromosphere is observed. This propagation of waves further con-

firms the theoretical consideration of chromospheric heating with waves in the presence of inclined fields. The energy fluxes derived are found to be $\sim 5 \times 10^6 ergscm^{-2}s^{-1}$ and $\sim 2.4 \times 10^6 ergscm^{-2}s^{-1}$ derived from cut-off frequencies, and $\sim 5.7 \times 10^6 ergscm^{-2}s^{-1}$ and $\sim 2.2 \times 10^6 ergscm^{-2}s^{-1}$ derived from travel times for the chromospheric heights I_{uv1} and I_{uv2}. These are comparable to the chromospheric radiative losses for the chromosphere in the quiet-Sun. This implies that the waves carry sufficient energy to heat the lower chromosphere. Even though the energy carried by these waves are more than enough to heat the lower chromosphere, we need to see the dissipation of energy of these waves in the chromosphere. For this purpose, multi-height data has to be considered to observe the decrease in energy of these waves at different heights is to be seen. In our analysis, we have carried out this at two different heights and have found that the energy of these waves is decreasing as the waves propagate to higher atmosphere. This dissipation of energy confirms that these are capable of heating the lower chromosphere.

5.2 Future directions

In this section, we briefly discuss the possible ways to expand the work already carried out in this thesis and its application to better understand the Sun with a particular interest in the surface magnetic fields. In each of the problems taken up, there are several promising avenues for future study. These and other plans specifically include:

1. The analyses carried out in Sangeetha & Rajaguru (2016) can be applied to magnetic regions in different dynamical states such as major atmospheric activities like eruptive events or flares. The dynamical effects of the evolution of magnetic fields before, during, and after these major atmospheric activities and their interactions with the fluid motions around them could be studied. Theoretical studies show that during the generation of the field, the dynamo mechanisms impart helicity to the fields and helicity is also imparted during the emergence of flux through the convection zone (Longcope et al., 1998). These interactions are assumed to be necessary for the observed pat-

terns on the surface (Liu et al., 2014b). The energetic flares appear in most complex magnetic structures. By repeating the analyses carried out in Sangeetha & Rajaguru (2016), one could probably have a more clearer picture on how these magnetic structures could affect these flares or post flare events.

2. In this thesis, we could not look into the aspects of helicity of the magnetic fields. Magnetic/current helicity quantifies how the magnetic field is sheared or twisted compared to its lowest energy state (Berger & Field, 1984). Observations provide evidence for the existence of such stresses in the solar magnetic field and their association with eruptive events are studied. The analyses carried out in Sangeetha & Rajaguru (2016) could also be performed for vertical components of current helicity. Since current helicity is derived from vector magnetic field measurements, accurate measurements of these fields are required. There have been reports on conflicting signs of currents helicity in the weak field regions due to lack of accurate measurements of vector magnetic fields (Gosain et al., 2013; Zhang, 2006). The recurrent explosive events, jets are found to occur with emergence and cancellation of the magnetic flux at the footpoints of the eruptions. The current helicity analysis carried out at these events could give more light on understanding what triggers such jets and eruptive events.

3. Energy fluxes carried by waves at upper photosphere and lower chromosphere are derived using phase-shifts between the photosphere and these heights as well as from cut-off frequencies in Chapter 4. Using the same analysis, a study of variation of energy fluxes of waves at different heights from lower chromosphere to corona can be calculated. The oscillatory power of the sunspot waves is found to trigger the recurrent jets observed. By calculating energy fluxes at various heights, the energy carried by these waves at different heights could give more insights on chromospheric and coronal heating as well as on the jet dynamics. This multi-height study would help in understanding the dissipation of energy carried by the p mode waves from the photosphere to corona (Fontenla et al., 1993).

Bibliography

Alfvén, H. 1947, *Mon. Not. Roy. Astron. Soc.*, 107, 211 13, 65

Anderson, L. S., & Athay, R. G. 1989, *ApJ*, 346, 1010 14

Avrett, E. 2000, Solar Atmosphere: Empirical Models, ed. P. Murdin 3

Balmaceda, L., Vargas Domínguez, S., Palacios, J., Cabello, I., & Domingo, V. 2010, *Astron. Astrophys.*, 513, L6 23

Bel, N., & Leroy, B. 1977, *Astron. Astrophys.*, 55, 239 64, 75

Bello González, N., Flores Soriano, M., Kneer, F., & Okunev, O. 2009, *Astron. Astrophys.*, 508, 941 72

Bello González, N., Flores Soriano, M., Kneer, F., Okunev, O., & Shchukina, N. 2010, *Astron. Astrophys.*, 522, A31 82

Berger, M. A. 1984, Geophysical and Astrophysical Fluid Dynamics, 30, 79 11, 50

Berger, M. A., & Field, G. B. 1984, Journal of Fluid Mechanics, 147, 133 9, 89

Biermann, L. 1946, Naturwissenschaften, 33, 118 65

Bogdan, T. J., Brown, T. M., Lites, B. W., & Thomas, J. H. 1993, *ApJ*, 406, 723 70

Bogdan, T. J., Carlsson, M., Hansteen, V. H., et al. 2003, *ApJ*, 599, 626 65

Bonet, J. A., Márquez, I., Sánchez Almeida, J., Cabello, I., & Domingo, V. 2008, *Astrophys. J. Lett.*, 687, L131 22

Borrero, J. M., Tomczyk, S., Kubo, M., et al. 2011, *Solar Phys.*, 273, 267 65

Brandenburg, A., Nordlund, A., Stein, R. F., & Torkelsson, U. 1995, *ApJ*, 446, 741 28

Brandenburg, A., & Schmitt, D. 1998, *Astron. Astrophys.*, 338, L55 47, 85

Brandenburg, A., & Subramanian, K. 2005, *Physics Reports*, 417, 1 10, 44, 85

Brandt, P. N., Scharmer, G. B., Ferguson, S., Shine, R. A., & Tarbell, T. D. 1988, *Nature*, 335, 238 22

Cally, P. S., & Bogdan, T. J. 1997, *Astrophys. J. Lett.*, 486, L67 65

Cally, P. S., Bogdan, T. J., & Zweibel, E. G. 1994, *ApJ*, 437, 505 65

Canfield, R. C., & Musman, S. 1973, *Astrophys. J. Lett.*, 184, L131 70

Centeno, R., Collados, M., & Trujillo Bueno, J. 2006, *ApJ*, 640, 1153 64

Chitta, L. P., Jain, R., Kariyappa, R., & Jefferies, S. M. 2012, *ApJ*, 744, 98 65

Couvidat, S., Rajaguru, S. P., Wachter, R., et al. 2012, *Solar Phys.*, 278, 217 14

De Moortel, I., & Rosner, R. 2007, *Solar Phys.*, 246, 53 77

De Pontieu, B., Erdélyi, R., & De Moortel, I. 2005, *Astrophys. J. Lett.*, 624, L61 64, 65

De Pontieu, B., Erdélyi, R., & James, S. P. 2004, *Nature*, 430, 536 64, 65

DeForest, C. E., Hagenaar, H. J., Lamb, D. A., Parnell, C. E., & Welsch, B. T. 2007, *ApJ*, 666, 576 7

Deubner, F.-L. 1975, *Astron. Astrophys.*, 44, 371 12

Domingo, V., Fleck, B., & Poland, A. I. 1995, *Solar Phys.*, 162, 1 15

Duvall, Jr., T. L., & Gizon, L. 2000, *Solar Phys.*, 192, 177 11, 23, 24, 37, 38, 51

Fan, Y. 2009, Living Reviews in Solar Physics, 6, 4 5

Felipe, T., Khomenko, E., Collados, M., & Beck, C. 2010, *ApJ*, 722, 131 64

Finsterle, W., Jefferies, S. M., Cacciani, A., et al. 2004a, *Solar Phys.*, 220, 317 65

Finsterle, W., Jefferies, S. M., Cacciani, A., Rapex, P., & McIntosh, S. W. 2004b, *Astrophys. J. Lett.*, 613, L185 65

Fontenla, J. M., Rabin, D., Hathaway, D. H., & Moore, R. L. 1993, *ApJ*, 405, 787 83, 85, 89

Fossum, A., & Carlsson, M. 2005a, *Nature*, 435, 919 64

—. 2005b, *ApJ*, 625, 556 67

Gizon, L., & Birch, A. C. 2005, Living Reviews in Solar Physics, 2, 6 23

Gizon, L., & Duvall, Jr., T. L. 2003, in ESA Special Publication, Vol. 517, GONG+ 2002. Local and Global Helioseismology: the Present and Future, ed. H. Sawaya-Lacoste, 43–52 11, 23, 24, 37, 38, 51

Goldreich, P., & Kumar, P. 1990, *ApJ*, 363, 694 64

Goode, P. R., Yurchyshyn, V., Cao, W., et al. 2010, *Astrophys. J. Lett.*, 714, L31 22

Gosain, S., Pevtsov, A. A., Rudenko, G. V., & Anfinogentov, S. A. 2013, *ApJ*, 772, 52 23, 46, 89

Hale, G. E. 1908, *ApJ*, 28, 315 4

—. 1927, *Nature*, 119, 708 10

Hart, A. B. 1954, *Mon. Not. Roy. Astron. Soc.*, 114, 17 8

Hindman, B. W., Haber, D. A., & Toomre, J. 2009, *ApJ*, 698, 1749 23

Hoeksema, J. T., Liu, Y., Hayashi, K., et al. 2014, *Solar Phys.*, 289, 3483 11, 14, 23

Hurlburt, N. E., Toomre, J., & Massaguer, J. M. 1986, *ApJ*, 311, 563 9

Innes, D. E., Genetelli, A., Attie, R., & Potts, H. E. 2009, *Astron. Astrophys.*, 495, 319 22

Jefferies, S. M., McIntosh, S. W., Armstrong, J. D., et al. 2006a, *Astrophys. J. Lett.*, 648, L151 64, 65, 72, 77, 82

Jefferies, S. M., McIntosh, S. W., Armstrong, J. D., et al. 2006b, in IAU Joint Discussion, Vol. 3, IAU Joint Discussion 64, 65, 82

Khomenko, E., & Cally, P. S. 2012, *ApJ*, 746, 68 65

Khomenko, E., & Collados, M. 2008, *ApJ*, 689, 1379 65

—. 2009, *Astron. Astrophys.*, 506, L5 65, 70, 75

Komm, R., Gosain, S., & Pevtsov, A. 2014, *Solar Phys.*, 289, 475 23

Komm, R., Howe, R., Hill, F., et al. 2007, *ApJ*, 667, 571 23

Krause, F., & Raedler, K. H. 1980, Mean-field magnetohydrodynamics and dynamo theory 10

Langfellner, J., Gizon, L., & Birch, A. C. 2015, *Astron. Astrophys.*, 581, A67 23, 28, 38

Leighton, R. B., Noyes, R. W., & Simon, G. W. 1962, *ApJ*, 135, 474 12

Lemen, J. R., Title, A. M., Akin, D. J., et al. 2012, *Solar Phys.*, 275, 17 15, 66

Lisle, J., & Toomre, J. 2004, in ESA Special Publication, Vol. 559, SOHO 14 Helio- and Asteroseismology: Towards a Golden Future, ed. D. Danesy, 556 28, 29

Lites, B. W. 1984, *ApJ*, 277, 874 64

—. 1988, *ApJ*, 334, 1054 64

Lites, B. W., White, O. R., & Packman, D. 1982, *ApJ*, 253, 386 64

Lites, B. W., Kubo, M., Socas-Navarro, H., et al. 2008, *ApJ*, 672, 1237 22

Liu, Y., Hoeksema, J. T., Bobra, M., et al. 2014a, *ApJ*, 785, 13 10, 50

Liu, Y., Hoeksema, J. T., & Sun, X. 2014b, *Astrophys. J. Lett.*, 783, L1 11, 23, 89

Longcope, D. W., Fisher, G. H., & Pevtsov, A. A. 1998, *ApJ*, 507, 417 10, 88

Loukitcheva, M., Solanki, S. K., & White, S. M. 2009a, *Astron. Astrophys.*, 497, 273 73

Loukitcheva, M. A., Solanki, S. K., & White, S. M. 2009b, in IAU Symposium, Vol. 259, Cosmic Magnetic Fields: From Planets, to Stars and Galaxies, ed. K. G. Strassmeier, A. G. Kosovichev, & J. E. Beckman, 185–190 73

Martínez González, M. J., Asensio Ramos, A., Arregui, I., et al. 2016, *ApJ*, 825, 119 50

Matloch, L., Cameron, R., Schmitt, D., & Schüssler, M. 2009, *Astron. Astrophys.*, 504, 1041

Maunder, E. W. 1904, *Mon. Not. Roy. Astron. Soc.*, 64, 747 5

McIntosh, S. W., & Jefferies, S. M. 2006, *Astrophys. J. Lett.*, 647, L77 64, 65

Moffatt, H. K. 1978, Magnetic field generation in electrically conducting fluids 10

Narain, U., & Ulmschneider, P. 1996, *Space Sci. Rev.*, 75, 453 65

Nordlund, Å., & Stein, R. F. 2001, *ApJ*, 546, 576 64

Nordlund, Å., Stein, R. F., & Asplund, M. 2009, Living Reviews in Solar Physics, 6, 2 22

Norton, A. A., Graham, J. P., Ulrich, R. K., et al. 2006, *Solar Phys.*, 239, 69 15

November, L. J., & Simon, G. W. 1988, *ApJ*, 333, 427 7, 26, 51

November, L. J., Toomre, J., Gebbie, K. B., & Simon, G. W. 1981, *Astrophys. J. Lett.*, 245, L123

Park, S.-H., Tsiropoula, G., Kontogiannis, I., et al. 2016, *Astron. Astrophys.*, 586, A25 50

Parker, E. N. 1955, *ApJ*, 121, 491 5, 10, 85

—. 1988, *ApJ*, 330, 474 65

—. 1991, *ApJ*, 376, 355 65

Pevtsov, A. A., Canfield, R. C., & Metcalf, T. R. 1995, *Astrophys. J. Lett.*, 440, L109 10

Proctor, M. R. E., & Weiss, N. O. 1982, Reports on Progress in Physics, 45, 1317 6, 33, 55

Rajaguru, S. P., Couvidat, S., Sun, X., Hayashi, K., & Schunker, H. 2013, *Solar Phys.*, 287, 107 26, 64, 65, 67, 75

Rajaguru, S. P., Sankarasubramanian, K., Wachter, R., & Scherrer, P. H. 2007, *Astrophys. J. Lett.*, 654, L175 75, 77

Rajaguru, S. P., Wachter, R., Sankarasubramanian, K., & Couvidat, S. 2010, *Astrophys. J. Lett.*, 721, L86 75, 77

Rieutord, M., & Rincon, F. 2010, Living Reviews in Solar Physics, 7, 2 9

Rijs, C., Rajaguru, S. P., Przybylski, D., et al. 2016, *ApJ*, 817, 45 70, 77

Rogachevskii, I., & Kleeorin, N. 2000, *Phys. Rev. E*, 61, 5202 44

Rüdiger, G. 2001, in IAU Symposium, Vol. 203, Recent Insights into the Physics of the Sun and Heliosphere: Highlights from SOHO and Other Space Missions, ed. P. Brekke, B. Fleck, & J. B. Gurman, 152 11, 47

Rüdiger, G., Brandenburg, A., & Pipin, V. V. 1999, Astronomische Nachrichten, 320, 135 28

Rüdiger, G., Pipin, V. V., & Belvedère, G. 2001, *Solar Phys.*, 198, 241 11

Sangeetha, C. R., & Rajaguru, S. P. 2016, *ApJ*, 824, 120 51, 88, 89

Scherrer, P. H., Bogart, R. S., Bush, R. I., et al. 1995, *Solar Phys.*, 162, 129 15

Scherrer, P. H., Schou, J., Bush, R. I., et al. 2012, *Solar Phys.*, 275, 207 14, 34, 67

Schou, J., Scherrer, P. H., Bush, R. I., et al. 2012, *Solar Phys.*, 275, 229 14, 23, 66

Schunker, H., & Braun, D. C. 2011, *Solar Phys.*, 268, 349 67

Schunker, H., & Cally, P. S. 2006, *Mon. Not. Roy. Astron. Soc.*, 372, 551 73

Schüssler, M., & Vögler, A. 2008, *Astron. Astrophys.*, 481, L5 22

Schwarzschild, M. 1948, *ApJ*, 107, 1 65

Seehafer, N. 1990, *Solar Phys.*, 125, 219 10

Shelyag, S., Cally, P. S., Reid, A., & Mathioudakis, M. 2013, *Astrophys. J. Lett.*, 776, L4 22

Shercliff, J. A. 1971, Film Notes, National Committee for Fluid Mechanics Films, Education Development Center, Inc., MIT, USA 46, 59, 87

Simon, G. W., & Leighton, R. B. 1964, *ApJ*, 140, 1120

Simon, G. W., November, L. J., Ferguson, S. H., et al. 1989, in NATO Advanced Science Institutes (ASI) Series C, Vol. 263, NATO Advanced Science Institutes (ASI) Series C, ed. R. J. Rutten & G. Severino, 371 22

Stein, R. F., & Leibacher, J. 1974, *Ann.Rev. Astron. Astrophys.*, 12, 407 12

Stein, R. F., & Nordlund, Å. 1998, *ApJ*, 499, 914 9

—. 2001, *ApJ*, 546, 585 64

Stenflo, J. O. 1973, *Solar Phys.*, 32, 41 5

Stix, M. 2002, The sun: an introduction 4

Title, A. M., Tarbell, T. D., Topka, K. P., et al. 1989, *ApJ*, 336, 475 7

Tziotziou, K., Tsiropoula, G., Mein, N., & Mein, P. 2006, *Astron. Astrophys.*, 456, 689 64

Ulmschneider, P. 1990, in Astronomical Society of the Pacific Conference Series, Vol. 9, Cool Stars, Stellar Systems, and the Sun, ed. G. Wallerstein, 3–14 65

Ulmschneider, P., & Musielak, Z. 2003, in Astronomical Society of the Pacific Conference Series, Vol. 286, Current Theoretical Models and Future High Resolution Solar Observations: Preparing for ATST, ed. A. A. Pevtsov & H. Uitenbroek, 363 65

Ulrich, R. K. 1970, *ApJ*, 162, 993 12

van Driel-Gesztelyi, L., Démoulin, P., & Mandrini, C. H. 2003, Advances in Space Research, 32, 1855 50

Vernazza, J. E., Avrett, E. H., & Loeser, R. 1981, *ApJ, Suppl.*, 45, 635 14, 72

Wang, Y., Noyes, R. W., Tarbell, T. D., & Title, A. M. 1995, *ApJ*, 447, 419 22, 38

Wedemeyer-Böhm, S., Scullion, E., Steiner, O., et al. 2012, *Nature*, 486, 505 9, 22, 50

Welsch, B. T., Fisher, G. H., Abbett, W. P., & Regnier, S. 2004, *ApJ*, 610, 1148 7, 26, 51

Welsch, B. T., Abbett, W. P., De Rosa, M. L., et al. 2007, *ApJ*, 670, 1434 11

Wunnenberg, M., Kneer, F., & Hirzberger, J. 2002, *Astron. Astrophys.*, 395, L51 82

Zaqarashvili, T. V., Zhelyazkov, I., & Ofman, L. 2015, *ApJ*, 813, 123 50

Zhang, H., Sokoloff, D., Rogachevskii, I., et al. 2006, *Mon. Not. Roy. Astron. Soc.*, 365, 276 44

Zhang, M. 2006, *Astrophys. J. Lett.*, 646, L85 23, 89